6

Synthesis of the Seismic Structure of the Greater Alaska Region: Continental Lithosphere

Xiaotao Yang[1], Michael Everett Mann[2], Karen M. Fischer[2], Margarete A. Jadamec[3,4], Songqiao Shawn Wei[5], Gary L. Pavlis[6], and Andrew John Schaeffer[7]

ABSTRACT

Significant advances have been made over the past two decades in constraining the structure of the continental lithosphere in Alaska, particularly with the EarthScope USArray seismic data collection efforts. This chapter distills recent seismic models in Alaska and western Yukon (Canada) and relates them to major faults and tectonic terranes. We synthesize results from eight shear-wave velocity models and seven crustal thickness models. Through objective clustering of seismic velocity profiles, we identify six different velocity domains, separately for the crust (at the depth range of 10–50 km) and the mantle (at the depth range of 40–120 km). The crustal seismic domains show strong correlations with average crustal thickness patterns and the distribution of major faults and tectonic terranes. The mantle seismic velocity domains demonstrate signatures of major faults and tectonic terranes in northern Alaska, while in southern Alaska the domains are primarily controlled by the geometry of the subducting lithosphere. The results of this study have significant implications for the tectonics and geodynamics of the overriding continental lithosphere from the margin to the interior. This synthesis will be of interest to future studies of Alaska as well as other modern and ancient systems involving convergent margins and terrane accretions.

6.1. INTRODUCTION

Geologic observations over the past 40 years suggest that the Alaskan lithosphere has been assembled from a collage of fragments since the Mesozoic (Colpron et al., 2007; W. J. Nokleberg et al., 1994; Plafker & Berg, 1994; Silberling et al., 1994). These fragments make Alaska a type locality for the concept of terrane accretion (Colpron et al., 2007; Coney et al., 1980; Moore & Box, 2016; T. L. Pavlis et al., 2019). New seismic imaging results during the past two decades or so have provided fundamental constraints on the lithospheric structure of Alaska. In this study, we seek to shed new light on the structure of the continental lithosphere in Alaska and northwesternmost Canada by integrating the results of recent shear-wave velocity models and receiver function studies enabled by data from the EarthScope Transportable Array (TA). In this paper, EarthScope refers to the U.S. National Science Foundation program operated from 2003 to 2018. Our study area lies within a broad tectonic region that spans the southern margin, where the Pacific plate subducts beneath the North American

[1]*Department of Earth, Atmospheric, and Planetary Sciences, Purdue University, West Lafayette, IN, USA*

[2]*Department of Earth, Environmental, and Planetary Sciences, Brown University, Providence, RI, USA*

[3]*Department of Geology, University at Buffalo, Buffalo, NY, USA*

[4]*Institute for Artificial Intelligence and Data Science, University at Buffalo, Buffalo, NY, USA*

[5]*Department of Earth and Environmental Sciences, Michigan State University, East Lansing, MI, USA*

[6]*Department of Earth and Atmospheric Sciences, Indiana University Bloomington, Bloomington, IN, USA*

[7]*Geological Survey of Canada, Natural Resources Canada, Sidney, Canada*

Tectonics and Seismic Structure of Alaska and Northwestern Canada: EarthScope and Beyond, Geophysical Monograph 290, First Edition.
Edited by Natalia A. Ruppert, Margarete A. Jadamec, and Jeffrey T. Freymueller.

DOI: 10.1002/9781394195947.ch6
Companion website: www.wiley.com/go/Ruppert

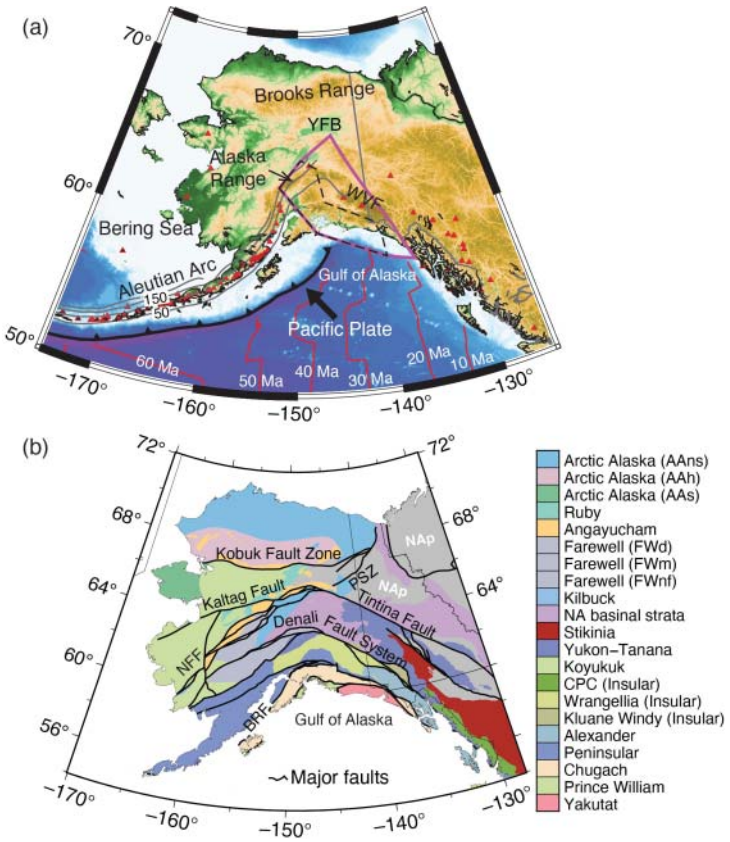

Figure 6.1 Tectonic settings of Alaska. (a) Key tectonic settings of Alaska, including the subduction of the Pacific Plate and the Yakutat microplate along the curved margin. Major topographic features are labels, including the Alaska Range, the Brooks Range, the Yukon Flats Basin (YFB), and the Wrangell Volcanic Field (WVF). The slab depth contours are from Slab2.0 (Hayes et al., 2018). The ages of the Pacific Plate are from Seton et al., (2020). The dashed black and solid magenta polygons mark the outlines of the Yakutat Microplate, the existence of which was originally proposed by Plafker et al., (1978), from Eberhart-Phillips et al. (2006) and G. L. Pavlis et al. (2019), respectively. Red triangles are active volcanoes. (b) Major terranes (color-shaded areas) and faults (thick lines) of the Canadian-Alaskan cordillera are from Colpron et al. (2007). Fault labels: PSZ, Porcupine Shear Zone; NFF, Nixon Fork-Iditarod Fault; BRF, Border Range Fault. Terrane labels: AAns, Arctic Alaska North Slope subterrane; AAh, Arctic Alaska Hammond-Coldfoot subterrane; AAs, Arctic Alaska Seward subterrane; FWd, Farewell Dillinger subterrane; FWm, Farewell Mystic subterrane; FWnf, Farewell Nixon Fork subterrane; CPC, Coast Plutonic Complex; NAp, North America platformal strata in western Laurentia.

plate, northward to the interior and the North Slope of Alaska (Figure 6.1a). From west to east, this convergent margin transitions from ocean–ocean subduction approximately west of 166°W longitude (Bird, 2003; DeMets et al., 1994; Müller et al., 2019; Seton et al., 2020; Tozer et al., 2019), through ocean–continent subduction from approximately 166°W to 144°W longitude (Bird, 2003; Jadamec & Billen, 2010; Müller et al., 2019; Plafker, Moore, & Winkler, 1994; Seton et al., 2020; Tozer et al., 2019), to a subduction–collision zone from approximately 144°W to 137°W longitude (Elliott & Freymueller, 2020; Enkelmann et al., 2010; Koons et al., 2010). In northern Alaska, the overriding lithosphere transitions from continental to oceanic, through a modern passive margin that leads into the Arctic Ocean and the Canada Basin (Grantz et al., 1994; Müller et al., 2019; Seton et al., 2020; Tozer et al., 2019).

This study focuses on the lithosphere of mainland Alaska and the western Yukon region. This region is comprised of a series of amalgamated tectonic terranes and large-scale faults (Figure 6.1b; Colpron et al., 2007; Koehler & Carver, 2018; Plafker & Berg, 1994). Some of the major fault systems in the study area include the Kobuk Fault Zone along the southern border of the Brooks Range in northern Alaska, the Kaltag and Tintina Faults in central Alaska, and the Denali Fault System

in southcentral Alaska (Plafker, Gilpin, & Lahr, 1994). These faults are primarily parallel to the arcuate plate margin (Figure 6.1b; Colpron et al., 2007). In addition, there are smaller-scale southwest–northeast trending faulting features, such as the Nixon Fork-Iditarod Fault and the Porcupine Shear Zone. For tectonic terranes, the Arctic Alaska terrane, with three subterranes, occupies most of the area north of the Kobuk Fault Zone and the Seward Peninsula. Western Alaska is dominated by the continental arc setting Koyukuk terrane and the accreted continental margin setting Farewell terrane (Figure 6.1b; Colpron et al., 2007). Eastern Alaska contains mostly the North America platformal and basinal terranes (Figure 6.1b; Colpron et al., 2007). The Wrangellia composite terrane dominates the Alaska region south of the Denali Fault System with accreted and displaced subterranes (Coney et al., 1980; Falkowski & Enkelmann, 2016). There are numerous fundamental questions remaining regarding the structure and tectonics of the continental lithosphere in the Greater Alaska region. Given Alaska's history of terrane accretion, how do the terrane boundaries and related faults correlate with present-day crustal and mantle lithospheric structure? How strongly does the geologic history of a terrane control its present-day crustal structure? How deep do the signatures of terrane accretion extend into the mantle lithosphere? What is the impact of the subducting-colliding Yakutat Microplate on the structure of the overriding plate? Understanding these questions requires comprehensive and objective knowledge about the deep structure of the lithosphere, building on top of the discovery from surface geology and tectonic studies. This motivates us to examine the relationship between crustal and mantle seismic structures and major faults and tectonic terranes.

The data from the EarthScope TA, together with other concurrent temporary seismic networks, have provided new constraints on the seismic and tectonic structure of the continental United States and Alaska. From 2005 to 2015, the TA was deployed across the contiguous United States from the active tectonic boundary in the west to the passive continental margin on the east coast. In 2015, the USArray Transportable Array began moving instruments to Alaska and westernmost Canada. This has dramatically improved the seismic data coverage in Alaska and western Yukon (Canada). Benefiting from the USArray TA records, there have been several seismic velocity and discontinuity models published in the past decade or so using different methods, parameters, and types of data (e.g., Ai et al., 2005; Allam et al., 2017; Audet et al., 2019; Berg et al., 2020; Brennan et al., 2011; Esteve et al., 2020; Esteve et al., 2021; Feng & Ritzwoller, 2019; Gama, Fischer, Dalton, & Eilon, 2022; Gama, Fischer, & Hua, 2022; Gou et al., 2019; Haney et al., 2020; Jiang et al., 2018; Kim et al., 2014; Liu et al., 2022; Mann et al., 2022; Martin-Short et al., 2018; Nayak et al., 2020; Rondenay et al., 2008, 2010; Rossi et al., 2006; Veenstra et al., 2006; Ward & Lin, 2018; Yang & Gao, 2020; Zhang et al., 2019). While sharing major seismic features, different models also reveal some unique seismic features that are only observed in certain models or a subset of the models. The inconsistency in seismic features among different models leads to uncertainties in characterizing coherent structural constraints and hinders the understanding of the geology and tectonics of Alaska. In this paper, we present a synthesis of seismic studies that utilize the seismic records from the EarthScope stations, focusing on extracting objective constraints from these results on the seismic structure of the lithosphere of the region. By combining eight shear-wave velocity models and seven crustal thickness models, we identify six different seismic domains, separately for the crust (at the depth range of 10–50 km) and the mantle lithosphere (at the depth range of 40–120 km). The crustal seismic domains show strong correlations with major faults and tectonic terranes. The mantle seismic domains demonstrate signatures of major faults and tectonic terranes in northern Alaska with a prominent reflection of the subduction structure in central and southern Alaska. The results of this study have significant implications for the tectonics and geodynamics of the overriding continental lithosphere from the margin to the interior.

6.2. DATA: COMPILATION OF SEISMIC MODELS

The study area spans the region from the subduction zone along the southern Alaska margin to the North Slope of Alaska bordering the Arctic Ocean. We focus on two types of seismic results for Alaska: (1) 3-D shear-wave velocity models of the crust and uppermost mantle and (2) thicknesses of the overriding crust. We exclude results that only cover the footprint of the Alaska Amphibious Community Seismic Experiment (Barcheck et al., 2020). We attempt to reveal common features in the models we used but not to compare and contrast detailed interpretations different authors made from their individual models. The readers are encouraged to read the corresponding publications summarized in Tables 6.1 and 6.2 for detailed descriptions of each individual seismic model we used. The seismic models synthesized in this study benefit from the data recorded by 29 seismic networks, as shown in Figure 6.2a. The network codes include 5C, 7C, AK, AT, AV, CN, II, IM, IU, PN, PO, PP, TA, US, XE, XF, XL, XM, XN, XO, XR, XV, XY, XZ, YE, YG, YM, YO, YV, Z5, and ZE. See the Availability Statement and Table S1 on the companion website for the descriptions and references corresponding to these network codes.

Table 6.1 Seismic shear-wave velocity models synthesized in this study (ordered by publication date).

Label	Data	Method	Depth (km)	Clusters	Reference
W2018	Surface waves from ambient noise and teleseismic P-wave receiver functions	Joint inversion	0 to 70	6	Ward and Lin (2018)
J2018	Surface waves from ambient noise and teleseismic P-wave arrival times	Joint inversion	0 to 800	6	Jiang et al. (2018)
M2018	Surface waves from ambient noise and earthquakes and teleseismic P-wave receiver functions	Joint inversion	0 to 200	5	Martin-Short et al. (2018)
F2019	Surface waves from ambient noise and earthquakes	Bayesian inversion	0 to 200	6	Feng and Ritzwoller (2019)
B2020	Surface waves from ambient noise and teleseismic P-wave receiver functions	Joint inversion	0 to 144	6	Berg et al. (2020)
Y2020	Surface waves from ambient noise	Full-wave tomography	0 to 150	5	Yang and Gao (2020)
N2020	Surface waves from ambient noise and body waves from earthquakes	Travel-time inversion	−1 to 300	6	Nayak et al. (2020)
G2022	Surface waves from ambient noise and teleseismic S-wave receiver functions	Joint inversion	0 to 226	5	Gama, Fischer, Dalton, & Eilon (2022)

Note: For the N2020 model by Nayak et al. (2020), we only consider the AKAN2020 model that covers the entire study area.

Table 6.2 Crustal thickness models synthesized in this study (ordered by the publication date).

Publication	Single-station estimates	Multi-station estimates	Data	Method
Veenstra et al. (2006)	X	–	P_S	Waveform fitting
Rossi et al. (2006)	X	–	P_S	H-κ stacking
Miller and Moresi (2018)	X	–	P_S	Hand-picked after post-stack migration
Zhang et al. (2019)	X	–	P_S	H-κ stacking
Haney et al. (2020)	–	X	Rayleigh wave phase velocity	Joint inversion for shear-wave velocity and crustal thickness
Mann et al. (2022)	X	X	P_S	2-D post-stack migration and 3-D CCP stacking
Gama, Fischer, and Hua (2022)	–	X	S_P	3-D CCP stacking

Notes: Mann et al. 2022 provide two sets of crustal thickness estimates: one for the continental crust beneath southeastern Alaska (Figure 6.6c) and the other for the thickness of the overriding crust above the subducting slab shallower than the intersection of the top of the slab with the overriding continental Moho (Figure S1 in the companion website, with instructions to access the supplementary information in the Availability Statement section). CCP, common-conversion-point stacking; P_S, P-to-S conversions; S_P; S-to-P conversions.

6.2.1. 3-D Shear-Wave Velocity Models

We collected eight representative 3-D shear-wave velocity models. Since the arrival of the EarthScope TA in Alaska, there have been a large number of velocity models published using data from the EarthScope TA stations and the Alaska regional network stations (e.g., Audet et al., 2019; Berg et al., 2020; Esteve et al., 2020; Esteve et al., 2021; Feng & Ritzwoller, 2019; Gama, Fischer, Dalton, & Eilon, 2022; Gou et al., 2019; Jiang et al., 2018;

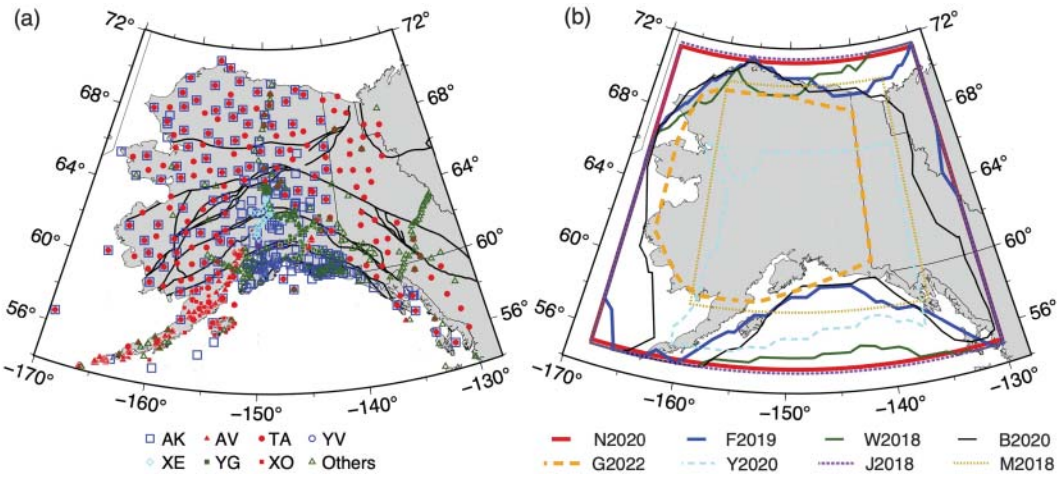

Figure 6.2 Seismic stations in Alaska and coverage of the seismic velocity models synthesized in this study. (a) Seismic stations from 29 networks between 2000 and 2022 that are used by the synthesized seismic models in this study. The station information is available through the IRIS Data Management Center and the International Federation of Digital Seismograph Networks. For simplicity in plotting, we plot the top seven networks, with the most stations, using different colors and symbols. Please see Table S1 on the companion website for the descriptions and references of all seismic networks plotted here. The thick lines are major fault traces as in Figure 6.1b. (b) Outlines of the shear-wave velocity models that are defined as regions with available shear-wave velocities between 1 and 6 km/s. We use this velocity range to exclude unconstrained model grids. The outlines are estimated using the velocity model at the depth of about 30 km for all models. W2018, model by Ward and Lin (2018); J2018, model by Jiang et al. (2018); M2018, model by Martin-Short et al. (2018); F2019, model by Feng and Ritzwoller (2019); B2020, model by Berg et al. (2020); Y2020, model by Yang and Gao (2020); N2020, model by Nayak et al. (2020); G2022, model by Gama, Fischer, Dalton, & Eilon (2022). See Table 6.1 for more information about these velocity models.

Liu et al., 2022; Martin-Short et al., 2018; Nayak et al., 2020; Ward & Lin, 2018; Yang & Gao, 2020). To narrow down the velocity models for this synthesis work, we select velocity models that satisfy the following conditions: (1) cover most of mainland Alaska, (2) provide isotropic seismic velocities, (3) use part or all EarthScope TA data, (4) include surface wave data to aid with the vertical resolution, (5) are available as digital velocity models through IRIS Earth Model Collaboration or personal communications, (6) provide absolute velocities or perturbations with an explicitly known reference model, and (7) cover at least the continental crust in depth. With these criteria, we choose eight 3-D shear-wave velocity models using different datasets and imaging methods. The data types and tomographic imaging methods for all selected models are summarized in Table 6.1. Hereafter, we refer to these models with the labels as in Table 6.1. For simplicity and consistency in descriptions, we label each of the velocity models systematically with the initial of the last name of the first author and the year the model was published. Model F2019 (Feng & Ritzwoller, 2019) provides the vertically polarized shear-wave velocity, V_{SV}, and the radial anisotropy (in %), ξ. We compute the isotropic velocity, V_S, as the Voigt average of V_{SV} and horizontally (V_{SH}) polarized shear-wave velocities (Anderson, 1987), which can be expressed as

$$V_S = \sqrt{2V_{SV}^2/3 + V_{SH}^2/3}. \tag{6.1}$$

The radial anisotropy, ξ, can be derived using

$$\xi = 100(V_{SH} - V_{SV})/V_{SV}. \tag{6.2}$$

From Equation (6.2), we have

$$V_{SH} = (0.01\xi + 1)V_{SV}. \tag{6.3}$$

Substituting Equation (6.3) into Equation (6.1), we obtain

$$V_S = \sqrt{\frac{2V_{SV}^2 + (0.01\xi + 1)^2 V_{SV}^2}{3}}. \tag{6.4}$$

Using Equation (6.4), we could compute the isotropic velocity model with given V_{SV} and ξ.

The footprint of these stations covers the entire mainland Alaska region and the western Yukon (Canada) region. The EarthScope TA stations have a nominal spacing of about 85 km, while some places, such as central Alaska and the Wrangell Volcanic Field, are covered with denser regional arrays. Among the eight velocity models, the Y2020 model (Yang & Gao, 2020) covers only central and southern Alaska (Figure 6.2b) while the

M2018 (Martin-Short et al., 2018) and G2022 (Gama, Fischer, Dalton, & Eilon, 2022) models cover most of Alaska. The rest of the velocity models cover the entire Alaska region. The J2018 (Jiang et al., 2018), F2019 (Feng & Ritzwoller, 2019), B2020 (Berg et al., 2020), and N2020 (Nayak et al., 2020) models also cover western Yukon, Canada (Figure 6.2b). In addition to the uneven coverage, these velocity model files are all in different model grids with different grid spacing and ranges. To facilitate quantitative comparisons, we interpolate all velocity models onto the same 3-D grids with grid sizes of 0.2 and 0.1 in longitudinal and latitudinal directions and 2 km in depth. The choice of grid spacing is based on a trade-off between efficiency and the precision of cluster boundaries. When interpolating, we keep the maximum resolvable depth of the original model (Table 6.1).

Most of the selected velocity models share similar large-scale features showing the change of velocity structures from the subduction margin to the south, through the continental interior, to the passive margin to the north (Figures 6.3 and 6.4). At the depth of 24 km (Figure 6.3, most of the velocity models show low-velocity features below the Brooks Range in northern Alaska and higher velocities to the south in central Alaska (Figure 6.3a-b, d-e, and g-h). The models also consistently show relatively low velocities in western and eastern Alaska, and western Yukon (Canada). These velocity features can also be observed from M2018 (Figure 6.3c), though the overall velocity variation is much smaller than in other models. Y2020 does not cover the Brooks Range, though the increase in velocity from the southern margin to the interior is observed (Figure 6.3f). At the depth of 80 km (Figure 6.4), all velocity models show elongated high-velocity features parallel to the Aleutian volcano arc, corresponding to the subducting Pacific plate. However, these high-velocity features possess different velocities and are in various scales across the models. The slab-like high-velocity features have lower amplitudes in model M2018 and are less well-resolved horizontally in G2022. The upper mantle velocities in central Alaska are generally lower than the surrounding areas, particularly those north of the Kobuk Fault Zone below the Brooks Range and further north. Relatively high upper mantle velocities are shown in northeastern Alaska and western Yukon (Canada) in all models.

6.2.2. Crustal Thickness Models

Crustal thickness is a fundamental parameter in Earth science. In the analysis described in this section and the dataset provided with this paper, crustal thickness is defined as the difference between the Earth's surface and a nearly ubiquitous vertically localized velocity increase, i.e., the Mohorovičić Discontinuity (Moho), located somewhere within the upper 70 km of the Earth. Across Alaska, crustal thickness has been studied using seismic analyses for decades (e.g., Fuis et al., 2008; Woollard et al., 1960; Zhang et al., 2019). However, the recent TA deployment has greatly improved the coverage for estimating crustal thickness and allows for continuous analysis across the entire state. Here, we compare crustal thickness estimates across Alaska from various studies and combine a number of them to create an integrated crustal thickness data set for the region. We select and integrate the results from seven studies (Table 6.2) that explicitly measure crustal thickness across Alaska by determining the depth to a sharp velocity gradient, i.e., the Moho. The results from the selected studies can be split into two groups: single-station and multi-station estimates of crustal thicknesses (Table 6.2).

The single-station estimates (Mann et al., 2022; Rossi et al., 2006; Veenstra et al., 2006; Zhang et al., 2019) and an updated version of the crustal thicknesses of Miller & Moresi (2018) (obtained from M. Miller through personal communications) involve the analysis of teleseismic P-wave receiver functions, which are time series of converted S waves generated from passing teleseismic P waves (e.g., Langston, 1977). These studies yield one value of crustal thickness beneath each seismic station (e.g., Figure 6.5). The single-station estimates of crustal thickness based on S-wave receiver functions (e.g., Gama et al., 2021; O'Driscoll & Miller, 2015) are not synthesized in our study because the S-to-P conversion points lie significantly farther from the station than their P-to-S counterparts. This results in greater potential inaccuracy when representing crustal thickness with a uniform value. Additional estimates of crustal thicknesses in Alaska based on P receiver functions also exist (e.g., Ai et al., 2005; Allam et al., 2017; Brennan et al., 2011; Kim et al., 2014; Rondenay et al., 2008, 2010) but are not explicitly shown here, mostly because (1) their crustal thickness values were not digitally available, (2) they did not report crustal thicknesses by station, or (3) the regions they sample and their specific approaches are similar to one of the studies in Table 6.2. Audet et al. (2020) provide robust crustal thickness values from P-wave receiver functions in western Canada, but the study does not overlap much with our study area.

The multi-station estimates yield maps of crustal thickness beneath and between nearby stations (e.g., Gama et al., 2021; Haney et al., 2020; Mann et al., 2022), providing overlapping crustal thickness constraints (Figure 6.6). The crustal thickness maps from both Mann et al. (2022) and Gama, Fischer, and Hua (2022) were generated from back-projecting receiver functions to depth through a velocity model. Mann et al. (2022) used teleseismic P-wave receiver functions, and Gama, Fischer, and Hua (2022) used teleseismic S-wave receiver functions. The map from

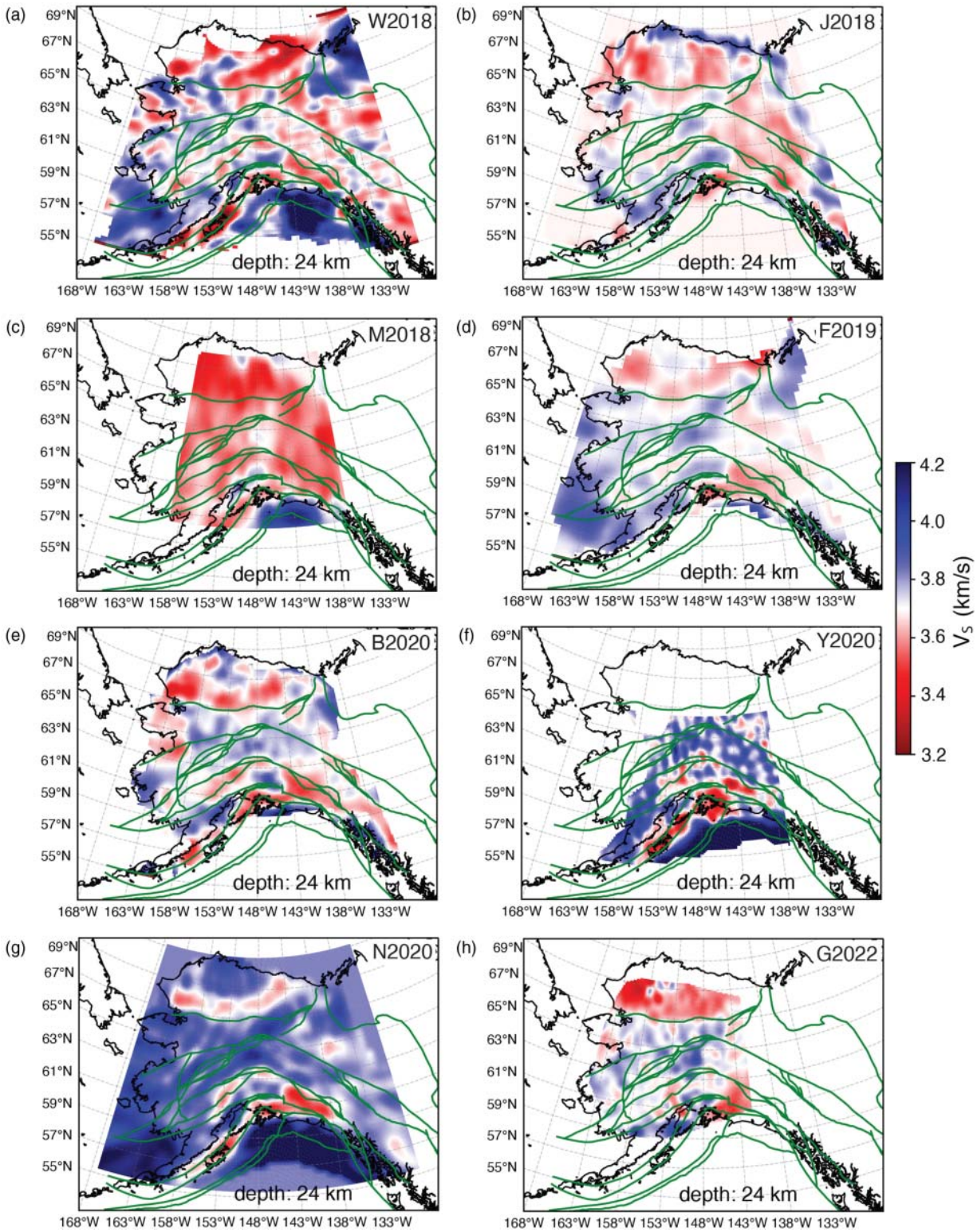

Figure 6.3 Examples of the synthesized shear-wave velocity models at the depth of 24 km. (a–h) Depth slices from models W2018 (Ward & Lin, 2018), J2018 (Jiang et al., 2018), M2018 (Martin-Short et al., 2018), F2019 (Feng & Ritzwoller, 2019), B2020 (Berg et al., 2020), Y2020 (Yang & Gao, 2020), N2020 (Nayak et al., 2020), and G2022 (Gama, Fischer, Dalton, & Eilon, 2022). Major faults (thick green lines) are shown for reference. After interpolations onto 0.2 (longitudes) by 0.1 (latitudes) grids, we smooth all models laterally over five grids for plotting.

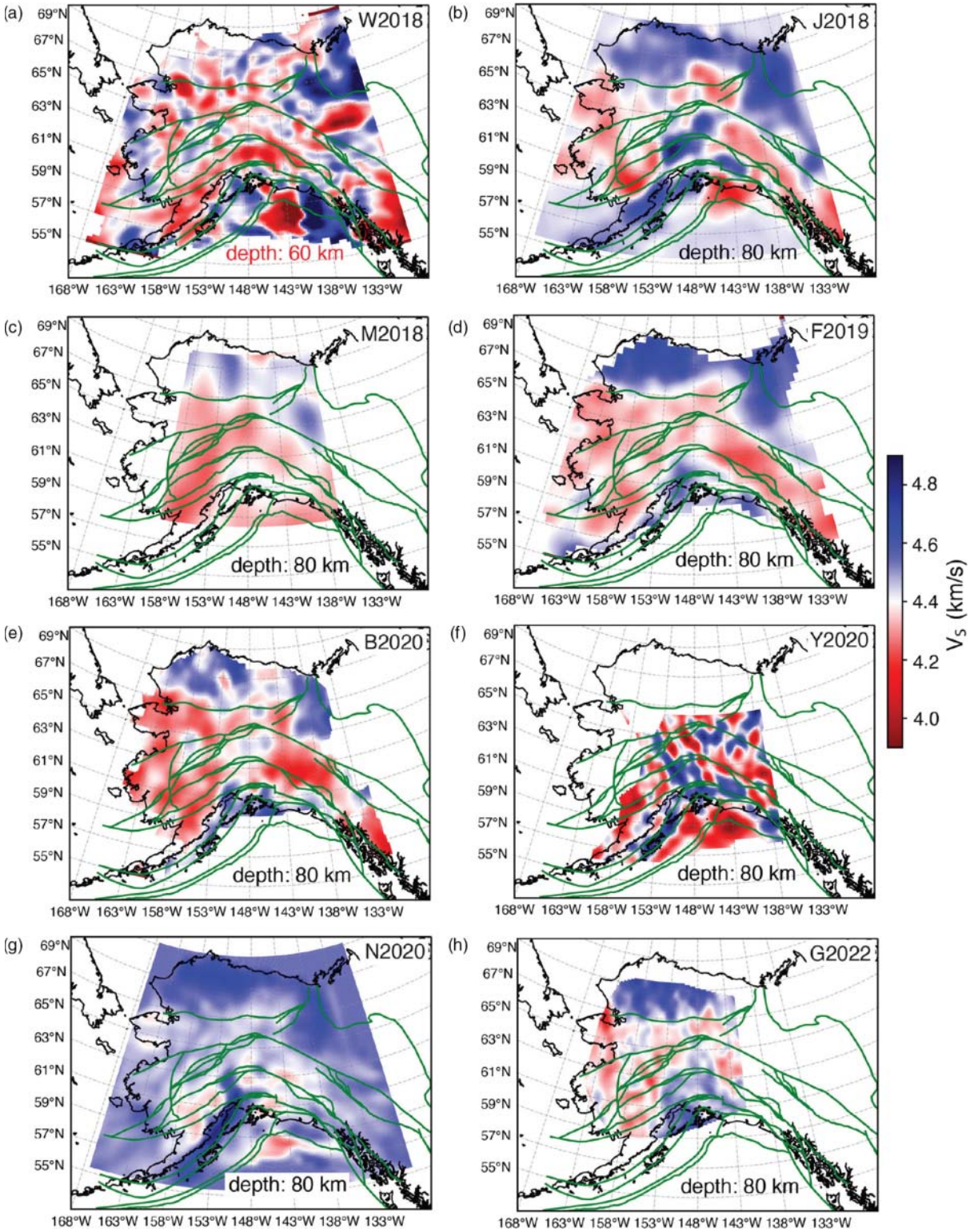

Figure 6.4 Same as Figure 6.3 but at the depths of 60 km for W2018 and 80 km for all other models. After interpolating onto 0.2 (longitudes) by 0.1 (latitudes) grids, we smooth all models laterally over five grids for plotting. See Figure 6.S2 on the companion website for the velocity maps at the depth of 60 km for all models.

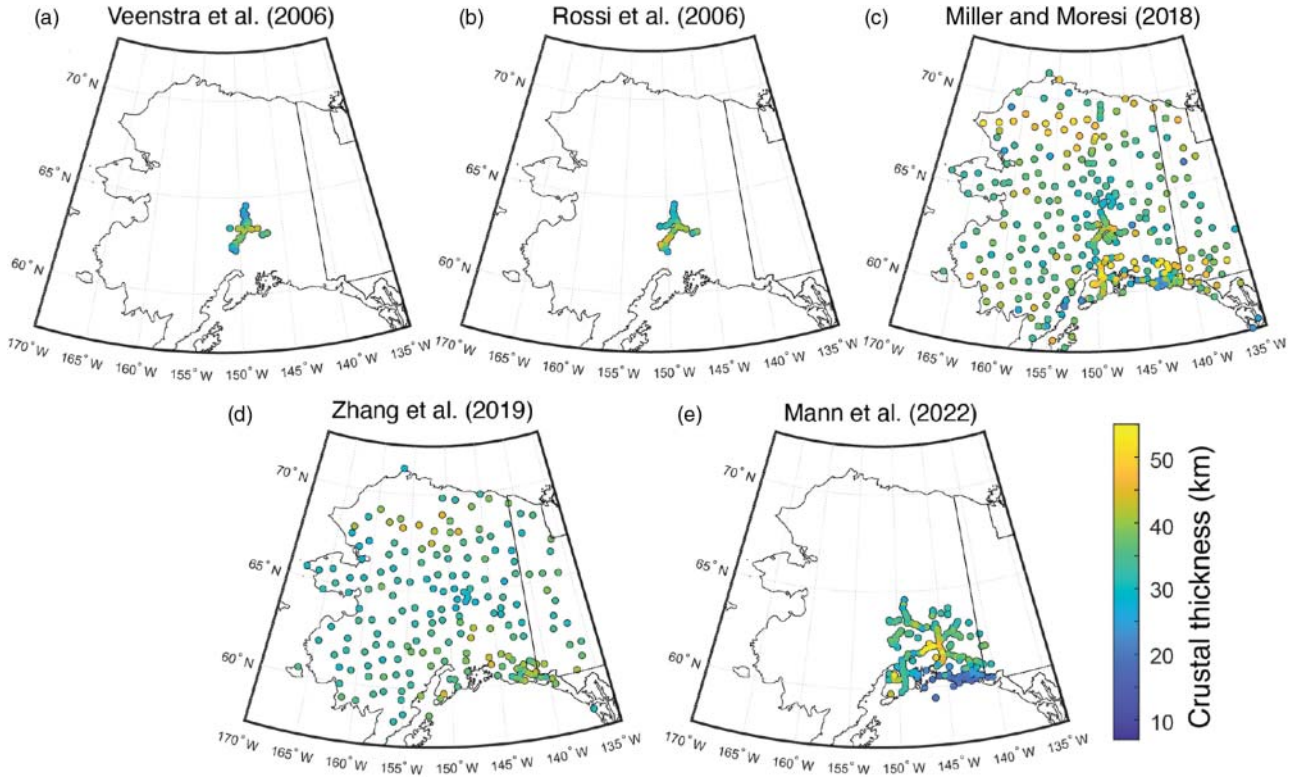

Figure 6.5 Single-station crustal thickness estimates from (a) Veenstra et al. (2006), (b) Rossi et al. (2006), (c) Miller and Moresi (2018), (d) Zhang et al. (2019), and (e) Mann et al. (2022).

Haney et al. (2020) was created using an inversion that solves for crustal thickness, as well as the shear velocity of the crust and an underlying mantle half-space, with an approximation based on the Dix equation to relate fundamental mode Rayleigh wave phase velocities to the velocity model. The criteria used in selecting these studies are: (1) they provide semicontinuous estimates of crustal thickness that were digitally available and (2) they employed EarthScope Transportable Array data.

In addition to the seven studies selected for this synthesis other approaches to measuring crustal thickness have also been applied in Alaska. Among studies that solve for 3-D velocity structure, those that jointly invert surface wave dispersion with P receiver functions (e.g., Berg et al., 2020; Feng & Ritzwoller, 2019; Martin-Short et al., 2018; Ward & Lin, 2018) or with S receiver functions (e.g., Gama, Fischer, Dalton, & Eilon, 2022; Gama et al., 2021) typically provide sharper resolution of the depth of the Moho velocity gradient than other approaches. However, the studies in these groups that sample mainland Alaska are represented in the analysis of shear-wave velocity models in Section 6.2.1, and their crustal thickness results are not explicitly considered in this section.

Among the selected studies (Table 6.2), the estimation of crustal thickness becomes complex in the southern part of the subduction zone, where the subducting crust is in contact with the overriding crust. In this case, there are typically multiple sharp velocity gradients as a function of depth (e.g., Bostock, 2013), including the Moho of the subducting plate, the base of the crust of the upper plate, and the interface between the two plates. Mann et al. (2022) mapped out the depth of the plate interface at depths <60 km (Figure 6.S1 on the companion website), which is available through the Zenodo repository as described in the Availability Statement. To approximately delineate the northern edge of the area where the Moho of the subducting plate is stacked beneath the crust of the upper plate, we use the plate interface depths of Mann et al. (2022) to determine the location of a line, referred to as the plate interface extent (PIE) line. This hypothetical line represents where the top of the slab intersects the base of the continental crust. For simplicity, we assume that this contact occurs at a depth of 40 km (Figure 6.S1 on the companion website), which is a reasonable approximation based on higher resolution velocity gradient profiles along lines of denser stations (Mann et al. 2022). In reality, the depth at which the top of the slab is in contact with the upper plate Moho varies, but accurately capturing this variation along the complete PIE line exceeds the resolution of existing studies. However, the 40 km contact depth is sufficient for our purposes since

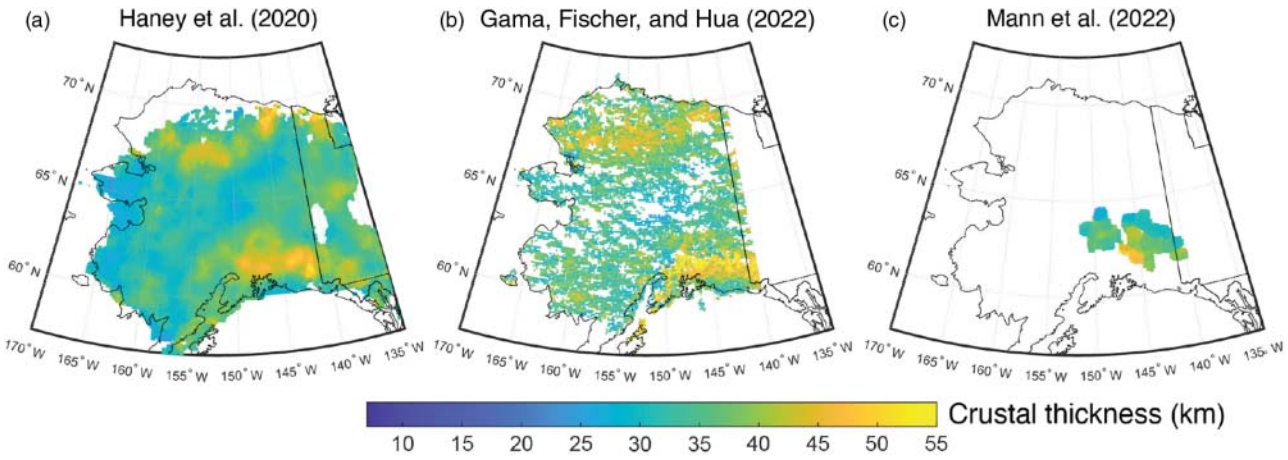

Figure 6.6 Multi-station continental crustal thickness estimates from (a) Haney et al. (2020), (b) Gama, Fischer, and Hua (2022), and (c) Mann et al. (2022).

the goal of the PIE line is simply to approximate where the continental crust is in contact with the subducting plate and multiple velocity gradients exist that obscure crustal thickness estimates. Mann et al. (2022) directly accounted for the multiple crustal velocity gradients when measuring the plate interface depth, which is equivalent to the thickness of the overriding continental crust south of the PIE line (Figure 6.S1 on the companion website).

Note that although we use the term plate interface extent, we emphasize that it is intended as a crust–crust contact in that it refers to the separation of the top of the crust of the downgoing plate from the base of the crust in the overriding plate. If there is any mantle lithosphere present in the overriding plate, then the top of subducting crust would be in contact with the mantle lithosphere at the base of the overriding plate north of the PIE line.

6.3. METHODS

To synthesize the two different types of models, i.e., the shear-wave velocity models and the crustal thickness models, we apply two categories of analyses. Considering lateral variations in the shear-wave velocity models, we use unsupervised K-means clustering of the 1-D velocity profiles to objectively analyze the regionalization of the 3-D velocity structure. This is also a way to reduce the dimension of the velocity models for the synthesis and has been effective in tectonic regionalization of global seismic velocity models (e.g., Eymold & Jordan, 2019; Lekic & Romanowicz, 2011; Schaeffer & Lebedev, 2015). For the crustal thickness models, we focus on the statistical analysis of all models by averaging the crustal thickness estimates. In the following paragraphs, we describe the details of the procedures for comparing and synthesizing the selected seismic models.

6.3.1. K-Means Clustering of 1-D Seismic Velocity Profiles

K-means clustering is commonly used to group data points based on their distances from the cluster centers. We use the *Tslearn* Python toolkit (Tavenard et al., 2020) for K-means clustering of time-series data to cluster the seismic velocity profiles (1-D depth profiles). The clustering operations are implemented as Python wrapper functions in the *SeisGo* toolbox (Yang, Bryan, et al., 2022; Yang, Zuffoletti, D'Souza, & Denolle, 2022). As described in Section 6.2.1, all velocity models are resampled onto the same 3-D grid with spacings of 0.2° in the longitudinal direction, 0.1° in the latitudinal direction, and 2 km in the depth direction. The resampled velocity models are clustered through the following steps (see Section 6.4.1 for the description of key observations):

Step 1: Determine the depth range for clustering. The velocity models to be analyzed have different depth ranges. This step sets the depth range of interest. From Figures 6.3 and 6.4 and Section 6.2.1, we observe varying velocity patterns from different velocity models, though they all show a lateral variation of velocities across Alaska and western Yukon (Canada). However, Figure 6.3 (as an example of crustal velocities) and Figure 6.4 (as an example of mantle lithosphere velocities) reveal different velocity features. Therefore, in this study, we divide the continental lithosphere into two depth ranges: 10–50 and 40–120 km. We use the minimum depth of 10 km to account for the lack of resolution at shallower depths in some of the velocity models, such as J2018 (Jiang et al., 2018), M2018 (Martin-Short et al., 2018), and Y2020 (Yang & Gao, 2020). Considering the overall crustal thickness within the study area (Section 6.2.2 and Figures 6.5 and 6.6), we use the depth range of 10–50 km to represent the

crust for clustering purposes. The depth of 120 km would include the total thickness of the upper plate lithosphere over most of the study area, with the exception of some of the thickest lithosphere in northern Alaska (Gama, Fischer, Dalton, & Eilon, 2022; Gama et al., 2021; Miller et al., 2018). However, in central Alaska, the lithosphere is much thinner (Gama, Fischer, & Hua, 2022), and a maximum depth of 120 km would also include the asthenospheric mantle. Hence, we use the depth range of 40–120 km for the mantle clustering analysis to capture variations in the structure of the mantle lithosphere of the continental plate while avoiding too much dilution of the lithospheric structure by the asthenospheric mantle.

Step 2: Choose the number of clusters for each velocity model. Specifying the number of clusters is required to run K-means clustering. To account for the different coverage of each velocity model, we choose six clusters for models that cover all of Alaska and the western Yukon (Canada) area, including W2018, J2018, F2019, B2020, and N2020 models (Figure 6.2b and Table 6.2). For models that only cover portions of the study area, including M2018, Y2020, and G2022, we choose five clusters (Figure 6.2b and Table 6.1). The clustering function in *SeisGo* (Yang, Zuffoletti, D'Souza, & Denolle, 2022) has the option of automatically determining the optimal number of clusters. For models in Table 6.1, the automatically determined numbers of clusters range from 5 to 8, resulting in small-scale clusters in some cases while producing similar major clusters as the results that use the preassigned number of clusters. Although the choice of the number of clusters is somewhat subjective, it does not change the overall conclusions of the analysis (Section 6.4).

Step 3: Smooth the 3-D velocity model and build an ensemble of 1-D velocity profiles. Due to the difference in data and methods, the selected velocity models may have different spatial resolutions. For instance, models W2018 (Ward & Lin, 2018) and Y2020 (Yang & Gao, 2020) show more small-scale features than other models (Figures 6.3 and 6.4). To focus on major velocity clustering patterns, we smooth all velocity models with a boxcar smoother across five grid points in both longitudinal and latitudinal directions but not in the depth direction. After smoothing the model, we build an ensemble of 1-D velocity profiles. The 1-D velocity profile at each longitude–latitude grid can be treated as a time series. This step generalizes the seismic velocity clustering into the clustering of a time-series data set.

Step 4: Conduct clustering of the ensemble of 1-D velocity profiles. We use the Euclidean distance as the distance metric in clustering. The clustering results are shown in Figures 6.7 and 6.8 for the depths of 10–50 and 40–120 km, respectively. The cluster labels are randomly assigned for each velocity model and are not directly comparable across different models. The cluster centers and the standard deviations are shown in Figures 6.S3 and 6.S4 for the depths of 10–50 and 40–120 km, respectively.

Step 5: Detect cluster boundaries. To compare the regionalization of the velocity structures from different models, we detect the boundaries between clusters from the clustering images that are color coded by the cluster labels (Figures 6.7 and 6.8). We compute the binary gradient around each resampled model grid or image pixel. The gradient is 0 if all four pixels have the same cluster label as the center pixel and 1 if there is at least one neighboring pixel in a different cluster, which means the center pixel is at a cluster boundary. The detected cluster boundaries for each velocity model are shown as red pixels in Figures 6.S5 and 6.S6 on the companion website for the clustering results at the depth of 10–50 and 40–120 km, respectively.

Step 6: Compute votes of cluster boundaries from all models. To highlight the cluster boundaries that are shared by multiple velocity models, we stack all images of the cluster boundaries and compute the total times a model grid (or image pixel) is detected as a cluster boundary. This step produces a vote map showing the distribution of cluster boundaries with all velocity models (Figure 6.9a-b). A higher vote means more models detect the cluster boundaries. From the vote maps of detected cluster boundaries, we identify the major velocity domains as outlined by cluster boundaries with $\geq$3 votes and extract the average velocity profiles within the domains (Figure 6.10). To minimize the bias, we pick cluster boundary lineaments and velocity domains solely based on the cluster boundary vote maps without referencing the fault lines and tectonic terranes.

6.3.2. Averaging of Crustal Thickness Estimates

We compute the average and standard deviation of crustal thicknesses separately for the compiled single-station and multi-station results (Table 6.2). For each station, we determine values that fall within grid nodes spaced 0.5° (longitude) by 0.25° (latitude) apart (Figures 6.11 and 6.S9 on the companion website). The choice of grid spacing is based on the typical station spacing in the study area (50–80 km). We adopt a two-step averaging approach, including taking the mean of values from a given study within the grid element and then taking the mean and standard deviation of the mean values from each study. This approach equalizes the influence of a given study within a grid element. For the multi-station crustal thickness map (Figure 6.11b), we use the plate

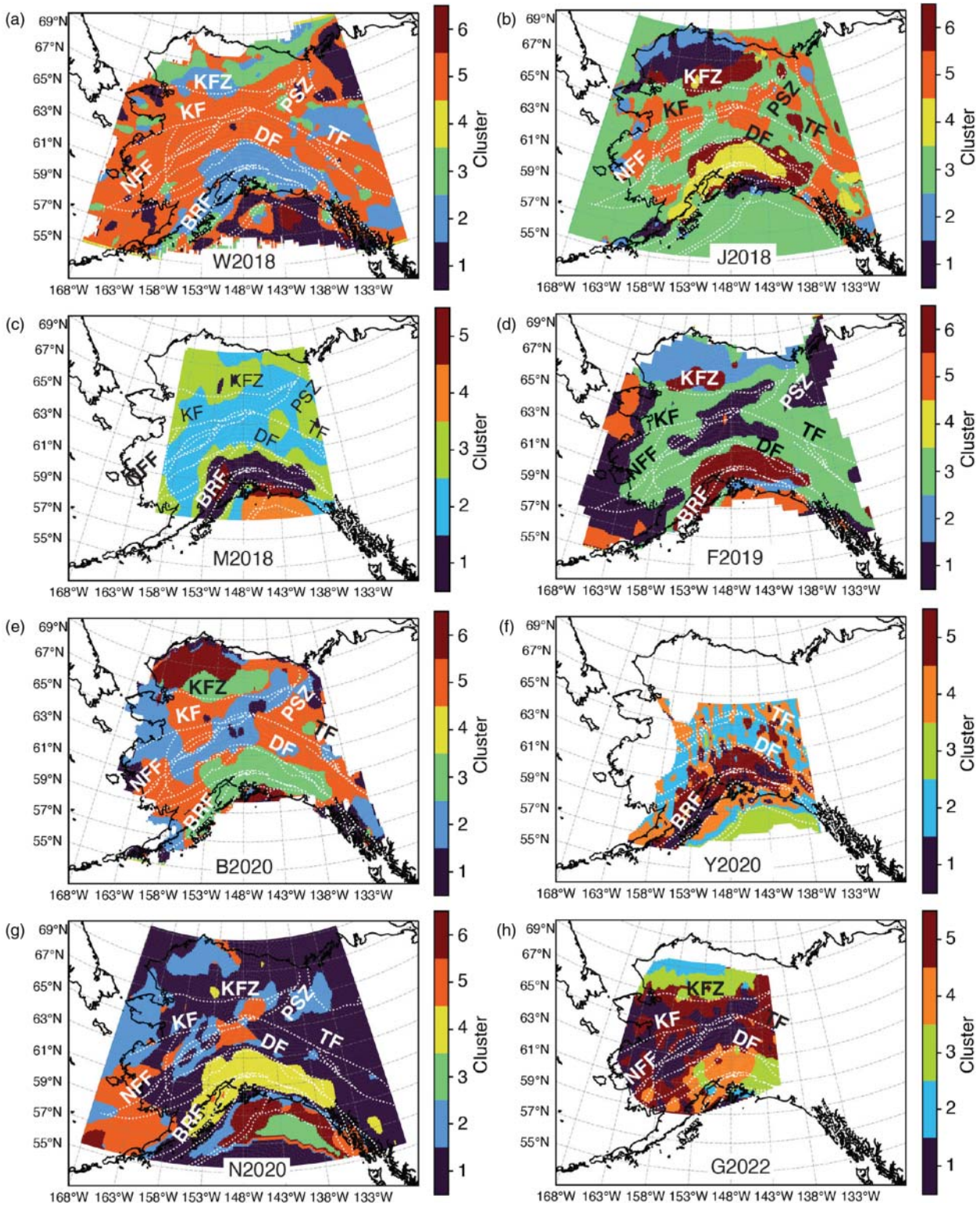

Figure 6.7 Clustering of velocity profiles between 10 and 50 km depths. The randomly-assigned cluster numbers are color-coded for each velocity model. The same cluster numbers for different velocity models may correspond to different velocity profiles. (a–h) Clustering results for models W2018 (Ward & Lin, 2018), J2018 (Jiang et al., 2018), M2018 (Martin-Short et al., 2018), F2019 (Feng & Ritzwoller, 2019), B2020 (Berg et al., 2020), Y2020 (Yang & Gao, 2020), N2020 (Nayak et al., 2020), and G2022 (Gama, Fischer, Dalton, & Eilon, 2022). The dotted white lines are the fault lines as in Figure 6.1b. Labels of major faults: KFZ, Kobuk Fault Zone; KF, Kaltag Fault; PSZ, Porcupine Shear Zone; NFF, Nixon Fork-Iditarod Fault; TF, Tintina Fault; DF, Denali Fault System; BRF, Border Range Fault.

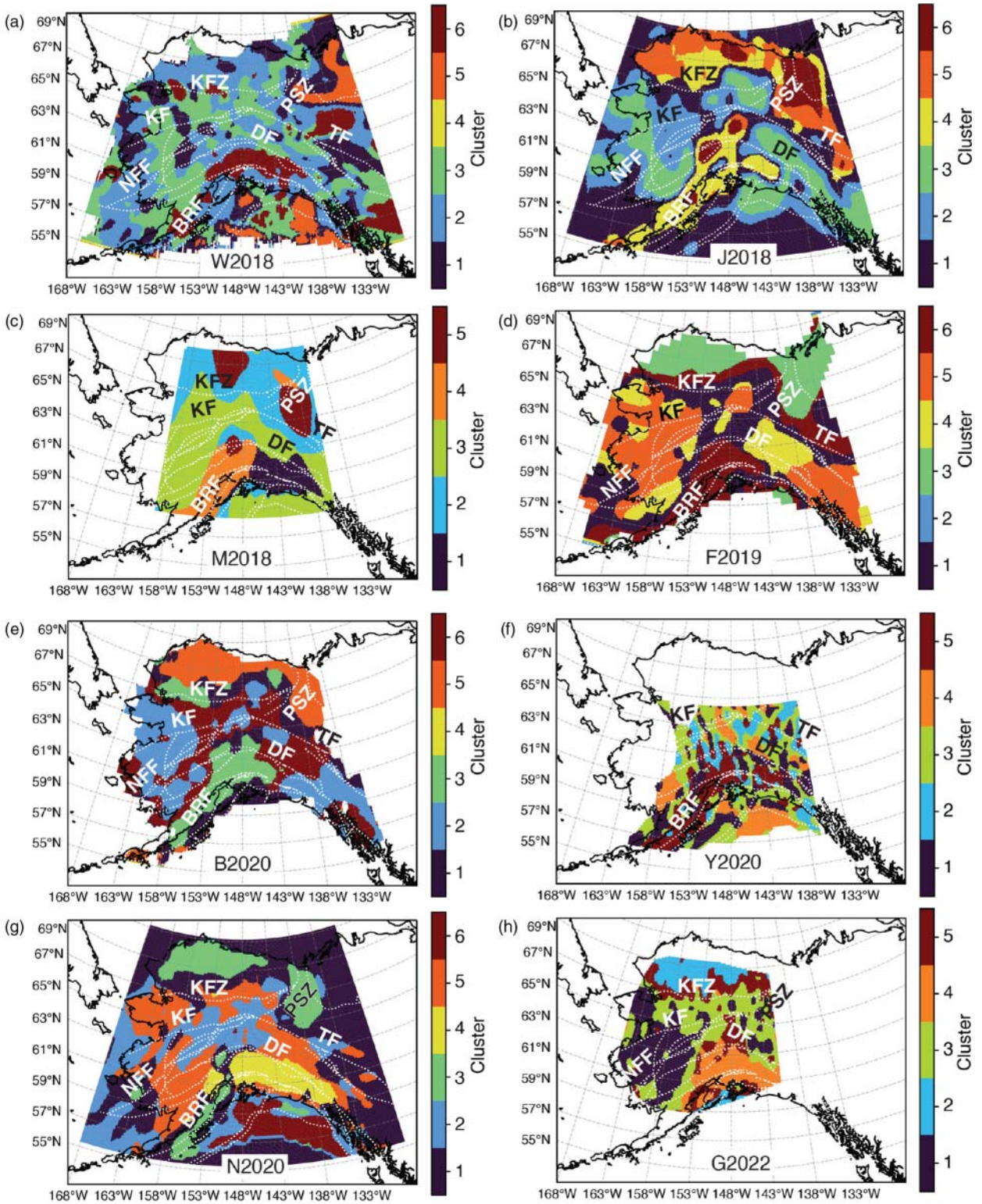

Figure 6.8 Same as Figure 6.7 but for velocity profiles at the depths of 40–120 km. The randomly assigned cluster numbers are color coded for each velocity model. The dotted white lines are the fault lines as in Figure 6.1b. See Figure 6.7 for the labels of major faults.

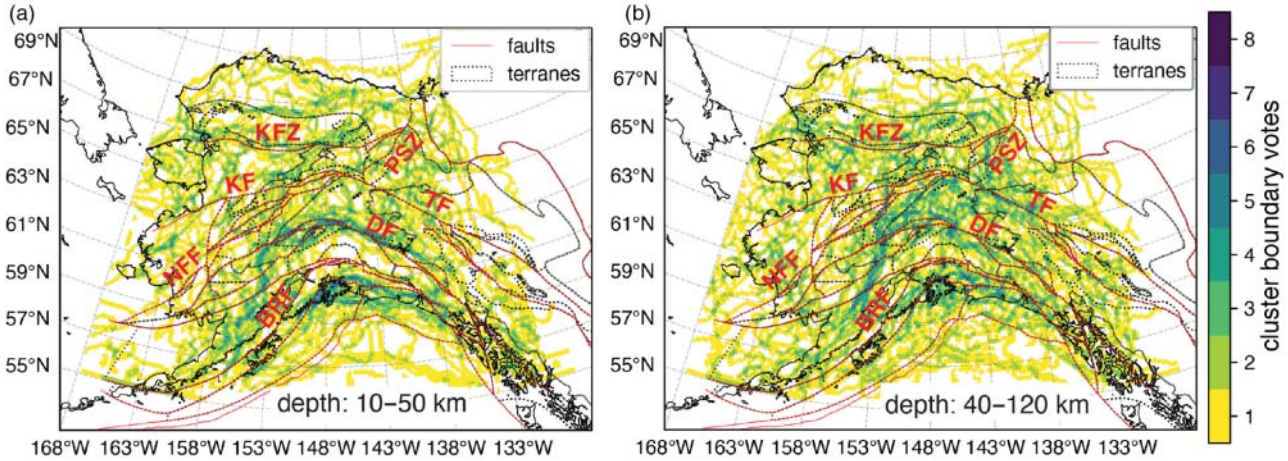

Figure 6.9 Detected cluster boundaries from all velocity models. (a, b) Cluster edge vote counts for the depths of 10–50 km and 40–120 km, respectively. Major faults (red solid lines) and terrane outlines (gray dotted lines) are shown for reference. See Figure 6.7 for the labels of major faults.

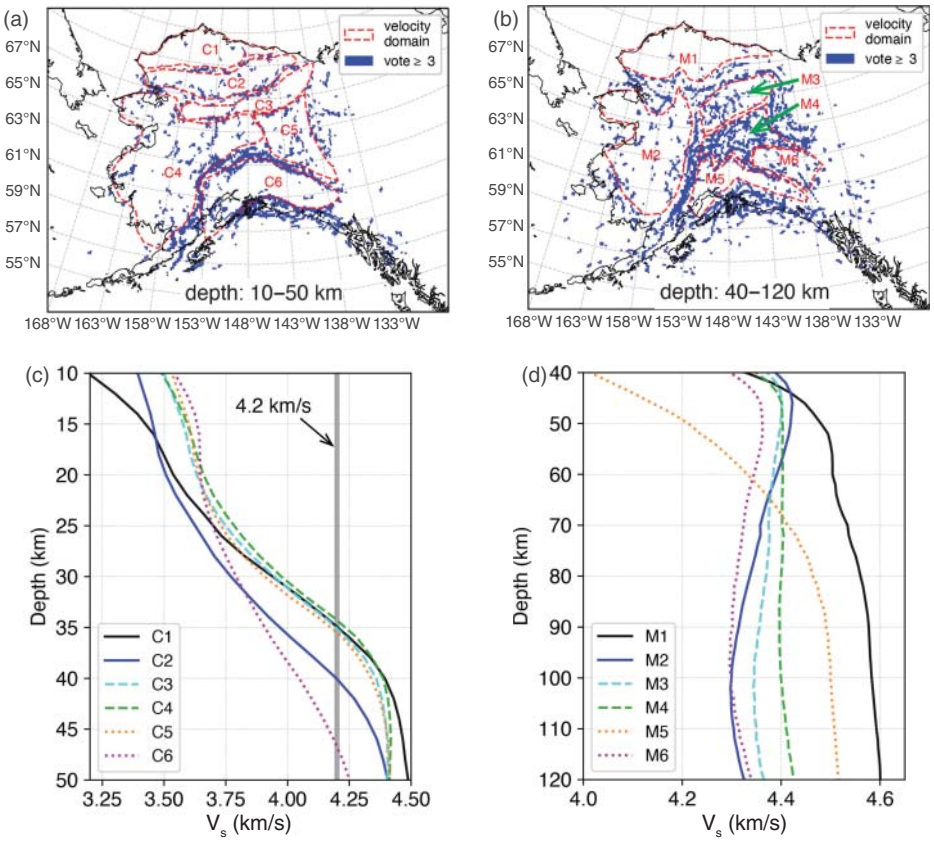

Figure 6.10 Major seismic velocity domains and the average velocity profiles. (a, b) Identified major velocity domains (alphanumerical labels C1–C6 and M1–M6 within the red dashed outlines) with ≥3 votes (blue pixels) for the depths of (a) 10–50 km and (b) 40–120 km. (c, d) Velocity profiles within each velocity domain averaged across all models at the depths of (c) 10–50 km and (d) 40–120 km. The thick gray vertical line in (c) is the V_S = 4.2 km/s line as the minimum velocity of melt-free ultramafic materials (e.g., Delph et al., 2021), which is used here as a proxy to denote the velocity at the bottom of the crust. See Figures 6.S7 and 6.S8 on the companion website for the velocity profiles from different velocity models for each velocity domain.

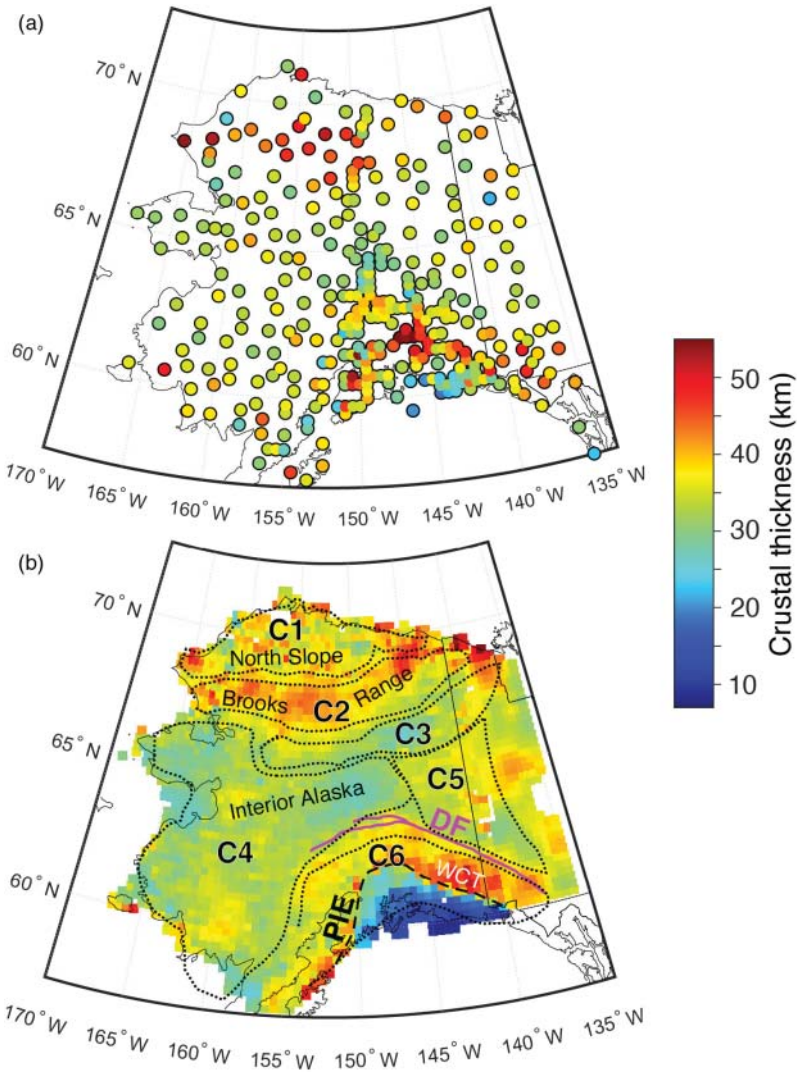

Figure 6.11 Average crustal thicknesses from multiple models. (a) Average of crustal thicknesses for single-station estimates. (b) Average of multi-station crustal thicknesses within each 0.5° (longitude) by 0.25° (latitude) bin. The dotted lines are outlines of the crustal seismic velocity domains as in Figure 6.10a, defined based on velocity clustering results. To the south of the plate interface extent (PIE) line, the map is showing the depth to the top of the subducting plate. DF, Denali Fault System; WCT, Wrangellia Composite Terrane.

interface depth from Mann et al. (2022) (Figure 6.S1 on the companion website) as the thickness of the overriding continental crust south of the PIE line, avoiding complexity due to the presence of both the upper-plate crust and the subducting crust. North of the PIE line, the crustal thickness simply corresponds to the mean Moho depth estimate, which is the base of the continental crust. When averaging crustal thicknesses, uncertainties in individual values are not taken into account, in part because not all studies report uncertainties. However, to estimate the potential impact of uncertainties in the input data, we also calculate the map of multi-station crustal thickness using uncertainties for each data point from the contributing studies as inverse weights at both stages of averaging. Gama, Fischer, and Hua (2022) provided a standard deviation for each crustal thickness value. Haney et al. (2020) estimated an uncertainty of 3.5 km for their crustal thicknesses, and an uncertainty of 3.0 km was estimated from the crustal thicknesses by Mann et al. (2022). Overall, these uncertainties place more weight on the values from Haney et al. (2020) and Mann et al. (2022). However, the resulting map of mean crustal thicknesses (Figure 6.S10a in the supplementary information) is very similar to the result without considering uncertainties (Figure 6.11b), and the differences are typically less than 1 km (Figure 6.S10b in the supplementary information).

6.4. RESULTS

6.4.1. Cluster Maps of Seismic Velocity Profiles

The clustering of crustal velocities (10–50 km) highlights the lateral variations correlated with major faults (Figure 6.7). In the cluster map of model W2018 (Figure 6.7a), the southern Alaska region south of the Denali Fault System is dominated by cluster 2. The region north of the Kobuk Fault Zone shows three clusters (2, 3, and 5). The western Yukon region is characterized by clusters 1, 2, and 5. The rest of the study area, mostly between the Kobuk Fault Zone and the Denali Fault System, is characterized by cluster 5. The clustering patterns from south to north across Alaska separated by the Denali Fault System and the Kobuk Fault Zone can also be observed from other models (Figure 6.7b–e and g–h). The cluster map of Y2020 (Figure 6.7f) also reveals the contrast in velocity patterns across the Denali Fault System although lacks coverage in northern Alaska. Models J2018, F2019, B2020, N2020, and G2022 also show the variation of velocity patterns/clusters from west to east across Alaska, as well as across the Porcupine Shear Zone in northeastern Alaska (Figure 6.7d, e, and g–h). In addition, the Pacific Plate in the northern Gulf of Alaska is characterized as separated clusters in models W2018 (clusters 1 and 6), M2018 (cluster 4), F2019 (cluster 5), Y2020 (cluster 3), and N2020 (clusters 3 and 6) with prominently higher velocities than the onshore area (Figure 6.S3 on the companion website).

The velocity clustering patterns in the mantle lithosphere (40–120 km) show correlations with both major faults and the subduction zone along the southern margin of Alaska (Figure 6.8). We observe separated clusters across the Kobuk Fault Zone (models W2018, J2018, F2019, B2020, N2020, and G2022 in Figure 6.8a,b, d,e, and g,h), the Porcupine Shear Zone (models W2018, J2018, M2018, F2019, B2020, and N2020 in Figure 6.8a–e and g), the Kaltag Fault (model N2020 in Figure 6.8g), the Denali Fault System from all models, and the Tintina Fault (models W2018, J2018, M2018, F2019, B2020, and N2020 in Figure 6.8a–e and g). However, some of the cluster boundaries only follow part of the fault lines. In southwestern Alaska, we observe elongated cluster regions subparallel to the subduction margin in multiple cluster maps, including the results from models J2018 (cluster 4), M2018 (cluster 4), F2019 (clusters 4 and 6), B2020 (cluster 3), Y2020 (cluster 5), N2020 (clusters 3 and 5), and G2022 (cluster 3). Most of these margin-parallel zones are located west of approximately 150°W in longitude. To the east, some models reveal a different cluster parallel to the margin, such as cluster 3 in J2018, cluster 1 in M2018, cluster 2 in B2020, cluster 4 in N2020, and cluster 4 in G2022. In Y2020, cluster 5 spans across the majority of the margin with a gap at around 145°W in longitude (Figure 6.8f). It is worth noting that parts of these margin-parallel cluster zones overlap with the crustal clusters to the south of the Denali Fault System (Figure 6.8d,e and g,h). Compared to the crustal cluster maps in Figure 6.7, the mantle cluster maps contain more small-scale variability, particularly those from models W2018 (Figure 6.8a), J2018 (Figure 6.8b), and G2022 (Figure 6.8h).

6.4.2. Major Velocity Domains Revealed by Cluster Boundaries

The vote maps of the velocity model cluster boundaries reveal major structural domains shared across multiple velocity models. The cluster boundaries from individual models show different patterns from model to model (Figures 6.S5-6.S6 on the companion website). However, by combining the detection of cluster boundaries from all models, the vote maps in Figure 6.9 highlight the cluster boundaries that are shared by multiple velocity models, shown as darker colors. Figure 6.10 shows the cluster boundary vote maps (blue pixels) with $\geq$3 votes. Due to the difference in spatial coverage of different models (Figure 6.2b), southern and central Alaska are sampled by all eight models, while other areas are sampled by at least five models. The threshold of 3 strikes a balance between highlighting major velocity domains shared by multiple models and having enough connectivity among pixels of the cluster boundaries to show major lineaments.

We identify six major velocity domains in the crust (C1–C6) and mantle lithosphere (M1–M6) defined by the cluster boundary lineaments (Figure 6.10a,b). These velocity domains outline major areas without noticeable lineaments of cluster boundary votes. Domain C1 overlaps with most of the area north of the Brooks Range in northern Alaska. C2 is mostly along the Brooks Range. Domains C3–C5 are located in the interior and western Alaska between the Brooks Range to the north and the Alaska Range to the south. C6 is located in southern Alaska covering the Alaska Range and the region to the south. For the mantle lithosphere, domain M1 spans across the Brooks Range and the North Slope area to the north. M2 occupies most of western Alaska and part of the interior. M3 is located to the southeast of M1 and to the east of M2. To the south, it is adjacent to domain M4, which is characterized by a group of small-scale cluster boundaries. To the south of M4, domains M5 and M6 are separated by a northwest–southeast trending cluster boundary lineament approximately along the Denali Fault System.

6.4.3. Velocity Profiles Within Major Domains

The average velocity profiles within the crustal velocity domains show similar overall patterns of increasing velocities with depth (Figure 6.10c). The velocities within domain C1 are lower than those within domains C3–C5 at the depths of <25 km. The velocities within domain C6 are lower than those for C3–C5 below the depth of 25 km. Domain C2 has velocities that are typically 0.2–0.3 km/s lower than other domains. The average shear-wave velocities reach 4.2 km/s at the depth of 35 ± 2 km within domains C1 and C3–C5, 40 ± 1 km within domain C2, and 45–46 km within domain C6. Domain C6 south of the Denali Fault System indicates the smallest velocity change over the entire depth range from 3.5 km/s to 4.25 km/s. In contrast, domain C1 shows the largest velocity range from 3.25 km/s to 4.5 km/s. However, there are notable variations across different velocity models for these domains (Figure 6.S7 on the companion website).

The mantle velocity domains show distinctly different average velocity profiles, particularly below the depth of 45 km (Figure 6.10d). Domain M1 has the overall highest velocity of 4.5–4.6 km/s below the depth of 50 km. Domains M2 and M6 both show a low-velocity zone at depths of about 60–120 km with a minimum velocity of 4.3 km/s at the depth of about 100 km. Domain M3 also contains a decrease in velocity at a similar depth range as M2 and M6 but with a lower amplitude. Below the depth of 45 km, domain M4 has the smallest overall velocity variation with an almost constant velocity of 4.4 km/s. Domain M5 shows the largest velocity variation of 0.5 km/s from 4 to 4.5 km/s. The velocity profile for domain M5 is also monotonically increasing, although the rate of increase becomes small below the depth of 90 km. Similar to the crustal domains, while we focus more on the average profiles, it is worth noting that the velocity profiles for the mantle domains also vary significantly across different models (Figure 6.S8 on the companion website).

6.4.4. Average Crustal Thickness

The average crustal thicknesses are shown in Figure 6.11a for the single-station averages and in Figure 6.11b for the multi-station averages north of the PIE line. The standard deviations in the single station estimates are much higher south of the PIE line than to its north (Figure 6.S9b), reflecting larger discrepancies among different studies in this region. This may result from the presence of multiple positive velocity gradients within both the upper plate and the shallowly dipping downgoing plate in this region, which includes the Yakutat crust. For example, different studies may have selected different positive velocity gradients below a given station as the Moho, resulting in discrepancies in inferred crustal thicknesses. South of the PIE line in the mean crustal thickness map from the multi-station estimates (Figure 6.11b), the upper plate crustal thickness is represented by the plate interface depth. North of the PIE line, the multi-station crustal thicknesses (Figure 6.11b) show a good agreement overall with the average of the single-station estimates (Figure 6.11a). However, in some locations, the average crustal thicknesses differ by more than 15 km. Some of these discrepancies are significant, in the sense that the standard deviations for the mean crustal thicknesses do not overlap. The Moho depth standard deviations north of the PIE line are typically lower for the multi-station crustal models (Figure 6.S9d) than for the single-station results (Figure 6.S9b), indicating more consistency across the individual multi-station crustal thickness models. Given this greater consistency and the more continuous lateral coverage provided by the multi-station models, we recommend the crustal thicknesses in Figure 6.11b as a reference model for continental Alaska.

We observe four notable crustal thickness patterns as revealed by the preferred reference model for Alaska (Figure 6.11b). (1) The crust across much of interior Alaska, approximately between the Alaska Range to the south and the Brooks Range to the north, is about 25–35 km thick, similar to the observations from previous studies (e.g., Ai et al., 2005; Allam et al., 2017; Brennan et al., 2011; Clarke & Silver, 1991; Gama, Fischer, Dalton, & Eilon, 2022; Gama et al., 2021; Gama, Fischer, & Hua, 2022; Haney et al., 2020; Mann et al., 2022; Martin-Short et al., 2018; Miller et al., 2018; Rossi et al., 2006; Searcy et al., 1996; Veenstra et al., 2006; Woollard et al., 1960; Zhang et al., 2019). (2) The Brooks Range in northern Alaska has a 40–50 km thick crust, which is similar to previous estimates (e.g., Fuis et al., 1995, 1997; Gama, Fischer, Dalton, & Eilon, 2022; Gama et al., 2021; Gama, Fischer, & Hua, 2022; Haney et al., 2020; Miller et al., 2018; Searcy et al., 1996; Woollard et al., 1960; Zhang et al., 2019). (3) The Wrangellia composite terrane in the south has a 35–55 km thick crust, as in previous studies (e.g., Fuis & Plafker, 1991; Gama, Fischer, Dalton, & Eilon, 2022; Gama, Fischer, & Hua, 2022; Haney et al., 2020). The crustal thickness of the Wrangellia composite terrane south of the Denali Fault System increases from 35 to >50 km from west to east. (4) A laterally sharp northward decrease in crustal thickness of about 10 km exists across the Denali Fault System, similar to the observations in previous studies (e.g., Allam et al., 2017; Brennan et al., 2011; Gama, Fischer, Dalton, & Eilon, 2022; Gama, Fischer, & Hua, 2022; Haney et al., 2020; Mann et al., 2022; Martin-Short et al., 2018; Miller et al., 2018; Rossi et al., 2006; Veenstra et al., 2006; Ward & Lin, 2018). This change in crustal thickness is most laterally localized at

the Denali Fault System between 140°W and 146°W. In the central segment of the Denali Fault System (at 146°W to 150°W), the decrease in crustal thickness is distributed across both the Denali and Hines Creek faults. Further to the west, the northward decrease in crustal thickness becomes lower in amplitude and/or more gradual and is less clearly associated with the Denali fault trace.

6.5. DISCUSSION

The patterns highlighted in Section 6.4 reveal major domains in terms of the integrated shear-wave velocity models (Figures 6.9 and 6.10) and crustal thicknesses (Figure 6.11). In this section, we place these results in the context of Alaskan tectonics and the evolution of the continental lithosphere.

6.5.1. Influence of Crustal Thickness on Velocity Clustering

The crustal velocity domains defined by the clustering of velocity profiles demonstrate a strong correlation with the crustal thickness patterns (Figure 6.11b). To examine the quantitative relationship between crustal thickness patterns and the velocity domains, we extract the average crustal thickness in each domain for both the crustal and mantle velocity domains (Figure 6.12). We also compare the crustal thickness within the crustal velocity domains with the depth along the average velocity profiles at a shear-wave velocity of 4.2 km/s, which is the minimum shear-wave velocity of melt-free ultramafic materials (e.g., Delph et al., 2021). Figure 6.12a shows that the depth to V_S = 4.2 km/s in domains C1–C5 is roughly similar to the average crustal thickness, following the reference line (slope = 1). The crustal thickness for domain C6 is about 36 ± 7.5 km, with a large error bar (Figure 6.12a,b). This may result from the fact that domain C6 spans across the PIE line, south of which the values are the depth to the plate interface, which dips to the north and thus varies significantly (Figure 6.11b). The same explanation is applicable to the crustal thickness for domain M5, which also has a large error bar (Figure 6.12c).

The clustering analysis in this study focuses on the holistic patterns of velocity profiles, and, thus, crustal thickness information is implicitly considered. Crustal thickness clearly plays a role in defining the crustal domains. For example, domains C1 and C2 have thicker crusts, relative to C3, C4, and C5, and the uncertainties for C2 and C4 do not overlap (Figure 6.12b). However, the difference in the internal velocity structure of the crust is also significant. For example, C1 and C2 have mean crustal thicknesses that differ by less than 3 km (Figure 6.12b), but these domains have contrasting velocity profiles, with C2 containing lower velocities in the crust below 20 km depth (Figure 6.10c). On the other hand, domains C3, C4, and C5 in the central latitudes of Alaska have similar crustal thicknesses and similar internal velocity structures. These cases highlight the fact that the average velocity profiles from all models (Figure 6.10c) oversimplify some aspects of the crustal structure. The boundaries of C3, C4, and C5 were defined using the velocity profile clusters from at least three individual studies (Figure 6.10a), indicating that contrasts in velocity profiles between these domains do exist in

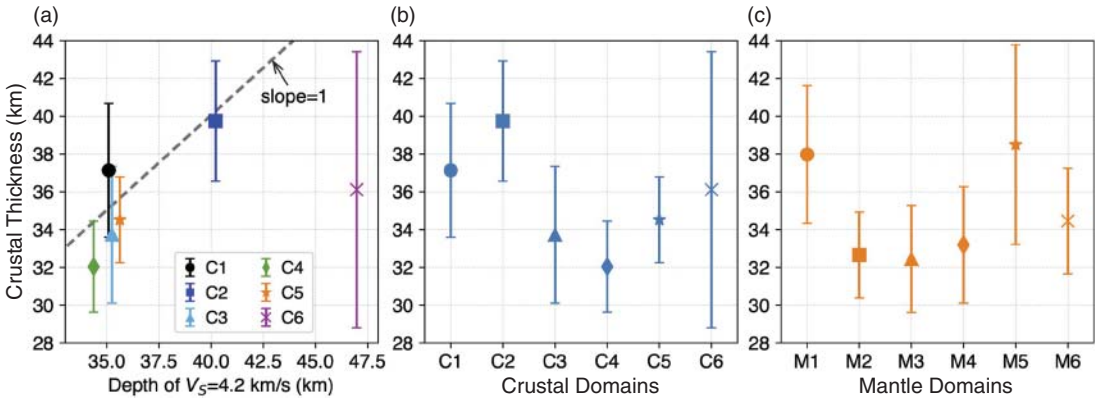

Figure 6.12 Crustal thicknesses within the crustal (C1–C6) and mantle (M1–M6) velocity domains using the multi-station average model in Figure 6.11b. (a) Comparison of crustal thicknesses within the crustal velocity domains (C1–C6) and the depths to the V_S = 4.2 km/s on the average velocity profiles in Figure 6.10c. The error bar shows the standard deviation of the crustal thicknesses within each domain. The dashed line, with a slope of 1, is plotted for reference. (b) Crustal thicknesses within the crustal velocity domains (C1–C6) as defined by clustering of the velocities at the depths of 10–50 km. (c) Crustal thicknesses within the mantle velocity domains (M1–M6) as defined by clustering of the velocities at the depths of 40–120 km.

some individual models. This result is backed up by the comparison of the cluster profiles for individual models (Figure 6.S7), which indicates more complicated internal velocity heterogeneity. However, when the profiles of all models are averaged (Figure 6.10c), some of these differences are less evident. Average crustal thicknesses are also shown for the mantle domains (Figure 6.12c). With velocities from depths of 40–120 km, the mantle velocity clustering should be much less influenced by the variation of crustal thicknesses, which are <40 km in most of the study area (Figure 6.11b).

6.5.2. Mantle Heterogeneity of the Seismic Domains

The mantle seismic structural domains possess distinctly different velocity structures, associated with varying lithospheric thicknesses, and in some cases with the influence of the subducting lithosphere. Comparison of the average velocity profiles in these domains indicates that mantle structure in Alaska can be divided into three broad domains: northernmost Alaska (M1), mantle containing subducting lithosphere in the south (M5), and everything in between (M2–M4 and M6).

Domain M1, in northernmost Alaska, is in a passive continental margin setting (e.g., Colpron et al., 2007; Müller et al., 2019), and its outline approximately matches the North Slope subterrane of the Arctic Alaska terrane (AAns in Figure 6.13a; Colpron et al., 2007; Plafker & Berg, 1994). The M1 domain is distinguished by the thickest mantle lithosphere with the highest velocity found in Alaska (Figure 6.10d), matching the conclusions of a wide range of studies (Berg et al., 2020; Feng & Ritzwoller, 2019; Gama, Fischer, Dalton, & Eilon, 2022; Gama et al., 2021; Gama, Fischer, & Hua, 2022; Jiang et al., 2018; Martin-Short et al., 2018; O'Driscoll & Miller, 2015). Heat flow is low relative to the rest of Alaska over much of the M1 domain, consistent with the low vertical thermal gradient in a thick mantle lithosphere (Batir et al., 2016). However, intriguingly, heat flow appears to increase in the northernmost tip of M1 (Batir et al., 2016). The M1 domain is also largely devoid of seismicity (Ruppert & West, 2020), suggesting little ongoing internal deformation. Most of the M1 domain lies beneath the relatively thick crust of the C1 crustal velocity domain, which is bordered by the thicker and lower-velocity crust of the C2 domain to the south (Figures 6.10 and 6.12b). The C2 domain largely corresponds to the Hammond-Coldfoot subterrane of the Arctic Alaska terrane (AAh in Figure 6.13a) and the moderately high topography of the Brooks Range. Overall, these observations are consistent with geologic information that the M1 domain/North Slope Arctic Alaska terrane represents an anomalous continental terrane (Colpron et al., 2007; Hubbard et al., 1987; Plafker & Berg, 1994; Strauss et al., 2013) that experienced crustal shortening and thickening at its southern margin during its accretion. However, the new information provided by the analyses of EarthScope TA data clearly shows that the mantle lithosphere of this terrane is as distinctive as its crust, based on its large thickness, high velocities, and apparently low temperatures.

The overriding lithosphere over most of the rest of Alaska is relatively thin. Domains M2–M4 and M6 show local minimum velocities at depths of 90–110 km, consistent with lithosphere that ends above this depth (e.g., Gama, Fischer, Dalton, & Eilon, 2022; Gama, Fischer, & Hua, 2022) (Figure 6.10d). The decrease of velocity for M4 within this depth range (90–110 km) is subtle but visible. This thinner lithosphere with an asthenospheric low-velocity layer is consistent with the higher heat flow observed in these domains (Batir et al., 2016). The lowest average asthenospheric velocities are observed in domains M2 and M6. M2 spans across the back-arc mantle of the main Alaska subduction zone. It reaches all the way to the Seward Peninsula where magmatic centers with decompression melting compositions occur (e.g., Mukasa et al., 2007). Domain M6, which also manifests the lowest average mantle lithospheric velocities, is located to the northeast of the Wrangell Volcanic Field. It may also reflect melting in the back-arc mantle to the northeast of the Wrangell slab, characterized by the dipping seismicity and slab-alike high velocities (Daly et al., 2021; Mann et al., 2022; Yang & Gao, 2020). The lower velocities could be explained by the mobile back-arc tectonics (Hyndman et al., 2005) or the toroidal return flow around the eastern Alaska slab edge (Jadamec & Billen, 2010, 2012). Domain M4 spans across the North America basinal strata and the Yukon-Tanana terrane (Figure 6.13b) with a nearly constant average velocity of 4.4 km/s in the mantle lithosphere (Figure 6.10d). The abundance of velocity cluster boundaries in M4 without clear lineaments (Figure 6.10b) suggests a highly heterogeneous mantle lithosphere in this region with strong lateral variations. M4 also overlaps with the northern corner of the shallowly subducting Yakutat Microplate (Figure 6.14; Finzel et al., 2015; Hayes et al., 2018; G. L. Pavlis et al., 2019), where a high-velocity body-wave anomaly is imaged (Figure 6.14). Additionally, M4 is located at the frontier of the Tintina Fault that intersects with the west–southwest to east–northeast trending Kaltag Fault (e.g., Audet et al., 2019; Esteve et al., 2020; Gabrielse et al., 2006). Therefore, the strong lateral heterogeneity in M4 likely reflects a complex and highly deformed mantle lithosphere related to Yakutat Microplate subduction and its impact on upper plate deformation.

In contrast to the other mantle domains, M5, which lies within the footprint of the subducting lithosphere,

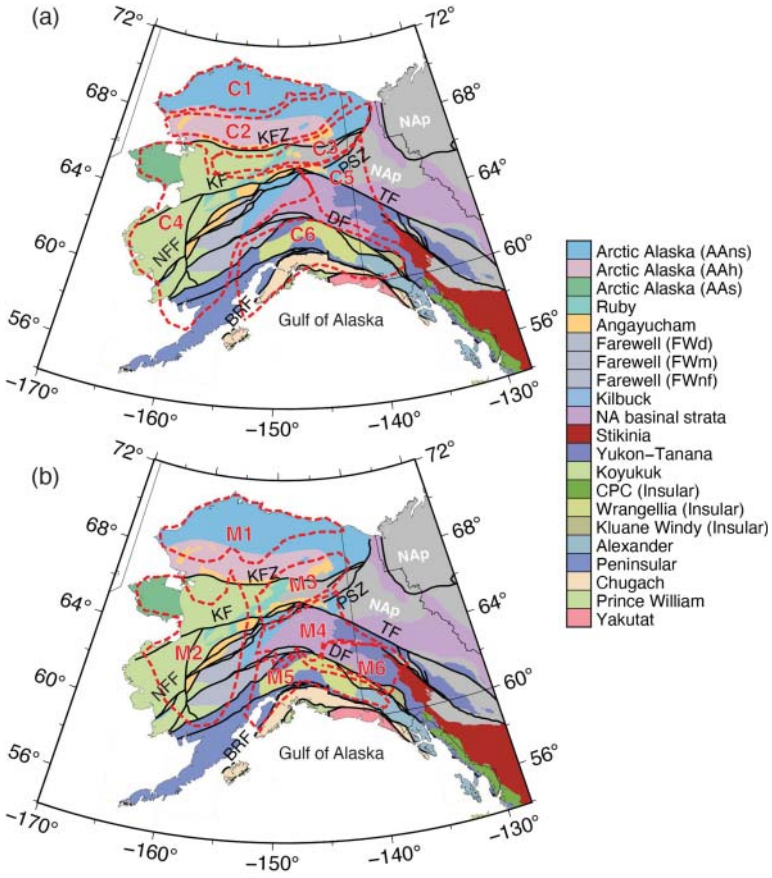

Figure 6.13 Comparison of velocity domains and major faults and tectonic terranes. (a) Major boundary lineaments of the velocity clusters (red dashed lines) and velocity domains (C1–C6) for 10–50 km clustering results overlapping on major fault lines and tectonic terrane maps. (b) Same as (a) but for mantle lithosphere at depths of 40–120 km (M1–M6). Labels of major faults are the same as in Figures 6.1b and 6.7 but are included here for easy reference. KFZ, Kobuk Fault Zone; KF, Kaltag Fault; PSZ, Porcupine Shear Zone; NFF, Nixon Fork-Iditarod Fault; TF, Tintina Fault; DF, Denali Fault System; BRF, Border Range Fault.

does not on average show evidence of a well-developed layer of high-velocity mantle lithosphere (Figures 6.10d and 6.14). Rather, velocities remain relatively low above the depth of about 55 km (Figure 6.10d), likely representing the vertical juxtaposition of the overriding crust and that of the subducting plate, where the latter largely comprises a thick Yakutat oceanic plateau (e.g., Chuang et al., 2017; G. L. Pavlis et al., 2019; Rondenay et al., 2010). The continued velocity increase likely represents the transition to the mantle of the subducting plate, which dominates the average velocity profile down to depths of 120 km (Figure 6.10d).

6.5.3. Correlation of Seismic Domains with Tectonic Features

Many of the most prominent boundaries delineated by the clustering analysis of the velocity models strike approximately parallel to the trends of the tectonic terranes and major faults in Alaska (Figure 6.13). In southern Alaska, some of these trends are approximately east–west but concave to the south, parallel to the active convergent margin (e.g., domains C6 and M5). In northern Alaska, some structural trends are concave to the north (e.g., C1-C3), reflecting more ancient accretionary tectonic terranes. The velocity model clustering and crustal thickness analyses indicate that the Denali Fault System, the Kobuk Fault Zone, and potentially the Porcupine Shear Zone represent lithospheric-scale boundaries that separate regions with distinct seismic structures. In contrast, the relationships of the Kaltag and Tintina faults to crustal and mantle domains are more complex. These findings are described below.

The dextral strike-slip Denali Fault System in southern Alaska has long been the target of geophysical studies. With a well-documented 10-km northward thinning of the crust across the Denali Fault System and/or Hines Creek Fault (Figure 6.11b; Allam et al., 2017; Brennan

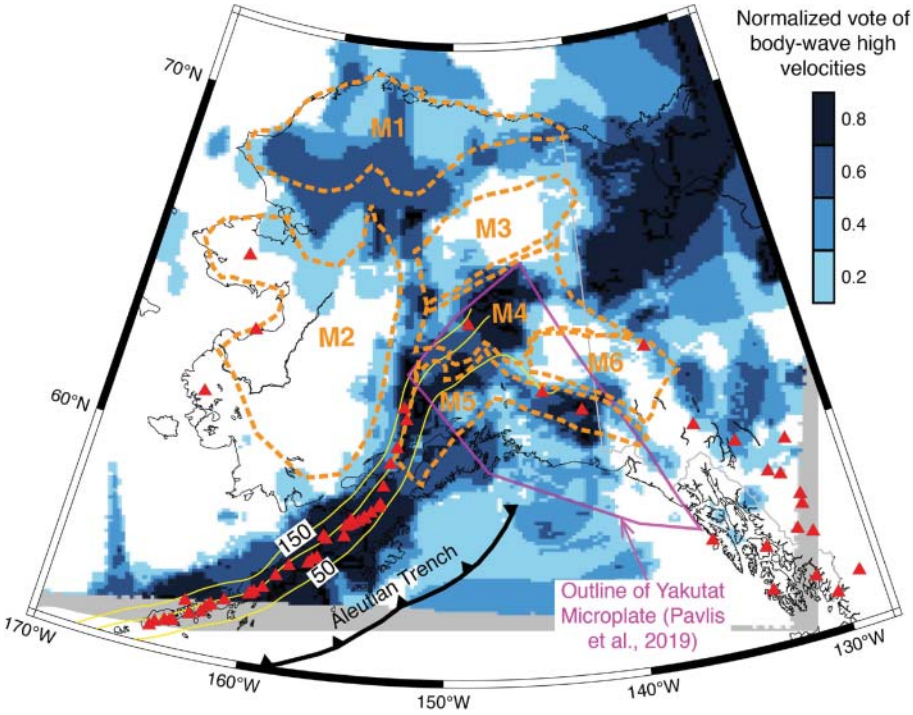

Figure 6.14 Comparison of mantle lithospheric velocity domains (M1–M6 within dashed outlines) and body-wave high velocities vote map at the depth of 100 km (colored background). The body-wave high velocities vote map is from Pavlis et al. (Chapter 8), which contains more details on the body-wave vote maps. The slab depth contours (yellow lines with labeled depths in km) are from Slab 2.0 (Hayes et al., 2018). The outline of the Yakutat Microplate (magenta polygon) is from G. L. Pavlis et al., (2019). The red triangles are the active volcanoes same as in Figure 6.1a.

et al., 2011; Gama, Fischer, Dalton, & Eilon, 2022; Gama, Fischer, & Hua, 2022; Haney et al., 2020; Mann et al., 2022; Martin-Short et al., 2018; Miller et al., 2018; Rossi et al., 2006; Veenstra et al., 2006; Ward & Lin, 2018), the overall Denali Fault System acts as a major crustal boundary that separates the Alaska Range and the Wrangellia composite terrane to the south and the North American affinity terranes in the interior of Alaska to the north (Benowitz et al., 2022; W. Nokleberg et al., 2013). High-resolution finite-element models of Alaska that incorporated a Denali fault lithospheric shear zone (Haynie & Jadamec, 2017; Jadamec et al., 2013) found a better fit to surface motion and regions of exhumation and subsidence in south-central Alaska than models that did not include a Denali fault shear zone (Jadamec & Billen, 2010, 2012). This suggests that the Denali Fault System may also represent a mantle structural boundary (Gama, Fischer, Dalton, & Eilon, 2022; Haynie & Jadamec, 2017; Jadamec et al., 2013; O'Driscoll & Miller, 2015). For example, recent work by Gama, Fischer, Dalton, and Eilon (2022) found a northward increase in total lithospheric thickness across the Denali Fault System, which in many places is accompanied by an increase in the shear-wave velocity of the mantle lithosphere.

The velocity clustering analysis in this study corroborates the view that the Denali Fault System is a major structural boundary in both the crust and the mantle (Figure 6.13). In the crust, the Denali Fault System aligns with the northern margin of domain C6. The fault-correlated transition in crustal structure delineated by the northern C6 margin is largely related to the well-documented decrease in crustal thickness across the Denali Fault System (e.g., Figure 6.11b and the previous paragraph), although contrasts in crustal velocity may also contribute. For example, at the depths of <20 km, the C6 crust (south of the Denali Fault System) has a slightly higher velocity than the crust of the C4 and C5 domains (north of the Denali Fault System). However, while the transition from the C6 to C4 or C5 domains does represent a significant change in crustal structure, the map of crustal thickness highlights that this transition is not uniform along the strike of the fault system. As noted in Section 6.4.4, the localization of the northward decrease in crustal thickness is most clearly correlated with the main trace of the Denali fault approximately east of 146°W. It is distributed across the Denali and Hines

Creek Faults between 146 and 150°W and becomes more gradual and less well correlated with the Denali Fault System west of 150°W. In the mantle, the Denali Fault System lies at the southern boundary of domains M4 and M6, where they transition to domain M5. The southern boundary of the M4 domain does not reach the western end of the Denali Fault System (Figure 6.13b). Instead, it terminates at the boundary that marks the eastern edge of the M2 domain at a longitude of approximately 153°W, which corresponds to the edge of the high-velocity subducting lithosphere (Figure 6.14). This relationship suggests that the cluster analysis in the 40–120 km depth range is strongly influenced by the subducting oceanic lithosphere in this region. To more directly assess mantle velocity contrasts across the Denali Fault System, where the overall lithosphere is relatively thin, velocity structure in the 50 to 90 km depth range should be examined. For example, in this depth range, Gama, Fischer, Dalton, and Eilon (2022) found northward thickening of the lithosphere and/or a southward increase in mantle velocity across the Denali Fault System at longitudes of 154°W and further east, while such mantle contrasts are less prominent across the Denali Fault further to the west.

The east–west trending Kobuk Fault Zone to the south of the Brooks Range in northern Alaska is currently the site of low-rate dextral strike-slip motion (Elliott & Freymueller, 2020) with a mix of faulting styles developed over time (Avé Lallemant et al., 1998). However, it has also been proposed as the ancient collisional boundary between the North Alaska Microplate to the north (including the North Slope and Hammond-Coldfoot subterranes) and the volcanic arc and other terranes to the south (Hubbard et al., 1987). The crustal thickness increases from 34 ± 3 km (C3) to 40 ± 3 km from south to north across the Kobuk Fault Zone (Figures 6.11b and 6.12b; Allam et al., 2017; Brennan et al., 2011; Clarke & Silver, 1991Fuis et al., 1995, 1997; Gama, Fischer, Dalton, & Eilon, 2022; Gama et al., 2021; Gama, Fischer, & Hua, 2022; Haney et al., 2020; Miller et al., 2018; Searcy et al., 1996; Veenstra et al., 2006; Woollard et al., 1960; Zhang et al., 2019). As described in Section 6.5.2, the velocity clustering results indicate that the Kobuk Fault Zone lies at the boundary of major velocity domains, including the C2–C3 and M1–M3 transitions (Figures 6.10a,b and 6.13). This observation is consistent with the view that lithospheric structural gradients help to localize deformation on this fault system.

To the southeast of the Brooks Range, the southwest–northeast trending Porcupine Shear Zone, with evidence of sinistral movement (von Gosen et al., 2019), is the boundary between the North Slope subterrane of the Arctic Alaska terrane (AAns in Figure 6.13) and the North America platformal strata in western Laurentia (NAp in Figure 6.13; Colpron et al., 2007). Although smaller in scale compared to the Kobuk Fault Zone and the Denali Fault System, the Porcupine Shear Zone appears to be the structural boundary between both the crustal and mantle velocity domains (C3–C5 in Figures 6.10a and 6.13a and M3–M4 in Figures 6.10b and 6.13b). It also lies at a gradient in crustal thickness (Figure 6.11b). Thus, the Porcupine Shear Zone is potentially a third strike-slip fault zone that connects to structural gradients in the mantle lithosphere.

In contrast, structural differences across the Kaltag Fault are primarily within the crustal range, while the structural signature of the Tintina Fault is primarily noticeable in the mantle lithosphere (Figure 6.13). The Kaltag Fault along the southern margin of the Brooks Range is a dextral strike-slip fault with more than 500 km slip in the late Cretaceous (Jones, 1980). Together with the Porcupine Shear Zone to its northeast, the Kaltag Fault has played an important role in the tectonic evolution of the Arctic Ocean Basin (Jones, 1980). The velocity domains C3 and C4 are separated by a lineament of cluster boundaries along the eastern section of the Kaltag Fault, to the east of longitude 155°W (Figures 6.10a and 6.13a). This is also the section with different tectonic terranes on the two sides of the fault (Figure 6.13a). The structural contrast further west across the fault is ambiguous, which is consistent with the fact that both sides of the fault belong to the same Koyukuk tectonic terrane (Figure 6.13a).

The Tintina Fault in eastern Alaska and western Canada is a margin-parallel, dextral strike-slip fault zone with about 430 km horizontal displacement (e.g., Gabrielse et al., 2006). Audet et al. (2019) and Esteve et al. (2020) imaged a prominent contrast in seismic velocities in the upper mantle across the Tintina Fault in the western Yukon, suggesting the fault as a lithospheric-scale shear zone along the western margin of the North American continent. In the velocity clustering results, a small section of the Tintina Fault coincides with the northwest–southeast trending northeastern edges of the M4 and M6 mantle domains (Figure 6.13b). In the individual N2020, F2019, J2018, and W2018 models, an anomalously high-velocity mantle lithosphere lies beneath the Yukon Stable Block, which is referred to by Esteve et al. (2020) as the Mackenzie craton. It is a fragment of the North American Platform on the northeast side of the Tintina Fault. However, the fault does not align with crustal cluster boundaries (Figure 6.13a). In summary, our analyses suggest that contrast in seismic structure exist mostly across a segment of the Tintina Fault in the mantle. This result, however, does not rule out a more laterally persistent contrast of seismic velocities at specific depths since the clustering analysis considers the average pattern over the 40–120 km depth range.

Velocity domains C6 and M5 are both spatially correlated with the Wrangellia composite terrane, sampling both continental and oceanic lithosphere (Figure 6.13). At depths of 10–50 km, domain C6 contains varying amounts of both overriding crust and the oceanic lithosphere of the downgoing Yakutat Microplate. The average velocity below the depth of about 25 km is much lower than those for the adjacent C4–C5 domains (Figure 6.10c). This might be attributed to the inclusion of the overriding crust and the underlying thick (up to 25 km) oceanic crust of the downgoing Yakutat Microplate (Bauer et al., 2014; Chuang et al., 2017; Eberhart-Phillips et al., 2004; Mann et al., 2022; Rondenay et al., 2010; Yang & Gao, 2020), resulting in combined crustal thicknesses that reach 55 km (Figure 6.11). As previously discussed (Section 6.5.2), at depths of 40–120 km in the M5 domain, the lower velocities than in other domains above the depth of 55 km likely reflect the thicker crust (Figure 6.10d), while the monotonically increasing velocities at greater depths sample mostly the oceanic mantle lithosphere (Gama, Fischer, & Hua, 2022; Mann et al., 2022; Rondenay et al., 2010; Yang & Gao, 2020). The northern boundaries of the C6 and M5 domains approximately align with the northern edge of a zone where P-wave receiver functions show anomalously strong azimuthal signals that are diagnostic of dipping fabrics, either dipping boundaries between isotropic layers or contrasts in P-wave velocity anisotropy where a plunging symmetry axis exists on at least one side of the interface (Schulte-Pelkum et al., 2020). This zone of intense dipping fabrics has been attributed to deformation related to subduction and oblique convergence (Schulte-Pelkum et al., 2020). Zones with prominent dipping fabrics also occur in portions of the C1 and M1 domains in northernmost Alaska (Schulte-Pelkum et al., 2020), but there the spatial variations in the intensity of the dipping fabrics are not well correlated with the C1 and M6 boundaries.

6.5.4. Implications for the Tectonics and Geodynamics of the Overriding Continental Lithosphere

This study reveals a number of seismic features of the Alaskan crust and mantle as highlighted by the shear-wave velocity model clustering and the integration of crustal thickness estimates. These seismic features shed light on the direction of future seismic, tectonic, and geodynamical studies, considering that variations in upper plate structure can have a first-order effect on both deformation in the overriding plate and the dynamics of the subducting slab (e.g., Haynie & Jadamec, 2017; Jadamec & Billen, 2012; Sharples et al., 2014).

One of the key findings from the synthesis is that some of the major faults and terrane boundaries spatially align with the margins of the crustal and mantle velocity domains that were independently determined from the velocity model clusters. Some of these correlations were previously documented, as in the case of the Denali and Kobuk faults (Allam et al., 2017; Brennan et al., 2011; Gama, Fischer, Dalton, & Eilon, 2022; Gama, Fischer, & Hua, 2022; Haney et al., 2020; Mann et al., 2022; Martin-Short et al., 2018; Miller et al., 2018; Rossi et al., 2006; Veenstra et al., 2006; Ward & Lin, 2018), but others, as in the case of the Porcupine Shear Zone, are newly revealed in this study. However, we have found that many boundaries of crustal and mantle velocity domains are not aligned. These results have the potential to add new constraints to tectonic models for how the complex mosaic of Alaskan terranes and faults interact (Bird, 1996; Elliott & Freymuller, 2020; Kalbas et al., 2008) and how they have evolved over time. A key next step will be to isolate how much of the mantle heterogeneity captured in the 40–120 km clusters actually lies within the mantle lithosphere versus the underlying asthenosphere or subducting plate.

In the case of northernmost Alaska, the southern boundary of the M1 domain corresponds to a lithospheric-scale feature that separates the anomalously thick and high-velocity mantle lithosphere beneath the North Slope Arctic Alaska terrane from the thinner lithosphere to the south. This observation poses a number of interesting questions. How has the North Slope M1 mantle lithosphere maintained its distinctive thickness and internal velocity structure over time? How much of the high mantle velocity is due to temperature, and how much could be attributed to mantle composition? A high-resolution model of mantle attenuation would be helpful in resolving this latter point, while the former requires input from geodynamic modeling efforts. Does the high velocity of the North Slope mantle actually signify a fragment of cratonic mantle lithosphere, as suggested in some studies (Gama, Fischer, Dalton, & Eilon, 2022), and does this indicate that the C1 domain is a remnant cratonic crust? The C2 domain, which contains the Brooks Range and lies over a transitional mantle with a variable lithospheric thickness, is comparable to many continental orogenic belts worldwide. How much does the anomalously thick and low-velocity (Figure 6.10c) C2 crust isostatically support the Brooks Range versus isostatic contributions from the mantle? Geodynamic modeling studies thus far have led to significant advances in understanding the tectonics of Alaska and the surrounding regions but much remains to be learned. Three-dimensional finite-element models spanning the entirety of mainland Alaska and northwestern Canada have incorporated a laterally variable lithospheric

structure in the overriding plate though focusing on the deformation in central and southern Alaska (Bird, 1996; Jadamec & Billen, 2010; Jadamec et.al., 2013; Kalbas et al., 2008). However, these models are limited by either not including the asthenosphere (e.g., Bird, 1996; Kalbas et al., 2008) or including the asthenosphere and part of the lower mantle but essentially fixing the North Slope region to the model boundary and, thus, limiting the lithospheric motion in northernmost Alaska (e.g., Jadamec & Billen, 2010; Jadamec et al., 2013). Other numerical models have included the deformation of northern Alaska using a thin viscous sheet approach (e.g., Finzel et al., 2015). However, the think viscous sheet models do not solve for flow in the asthenosphere or lower mantle. In the future, a more complete treatment of the North Slope region will aid in self-consistently assessing mantle flow and Brooks Range equilibrium, for example. Overall, the new EarthScope data and results will foster continued rich model development and geodynamic discovery in Alaska and northwestern Canada.

The alignment of some major fault systems (Denali, Kobuk, Porcupine Shear Zone, Kaltag, Tintina) with the margins of the crustal and/or mantle velocity domains also has the potential to provide new constraints on the depth extent and dynamics of strike-slip faulting in the continental lithosphere. Such correlations may indicate that lateral variations in the strength of the crust and mantle lithosphere play a role in determining and maintaining the location of the fault zone, as has been suggested globally (e.g., Molnar & Dayem, 2010; Dayem et al., 2009). The fault zones and the local reduction in strength that they represent in turn have a major impact on the dynamics of the overriding plate in Alaska (e.g., Haynie & Jadamec, 2017). For example, the Wrangell block, a region between the Alaska megathrust to the south and the Denali fault to the north, moves semi-independently from the inboard North American plate of interior Alaska (Lahr & Plafker, 1980). GPS data analyses indicate the northwest-directed counterclockwise motion of the Wrangell block and its subdomains (e.g., Elliott & Freymueller, 2020). Geodynamic modeling demonstrates that the subparallelism of the plate boundary corner with the inboard Denali fault allows northwest-directed flat slab subduction of the Pacific-Wrangell plate to drive the overriding Wrangell block from below, with the Denali fault strength modulating its rotation (Haynie & Jadamec, 2017; Jadamec et al., 2013). In the future, high-resolution studies of seismic velocity (both isotropic and anisotropic) in the vicinity of the major fault systems of Alaska have the potential to help constrain this process and the degree to which strike-slip deformation remains horizontally localized in the deep crust and mantle lithosphere.

The results of this study also highlight the significant effect of the subduction of the Yakutat terrane in southern Alaska, which is expressed as the thick crust evident in the C6 and the top of the M5 domains, and the structural complexity in the M4 domain. The average crustal velocity profile in the C6 domain (which reflects continental crust over the subducting plate) provides new constraints on the buoyancy of the Yakutat crust. These constraints will be useful for lithospheric-scale (e.g., Finzel et al., 2015; McConeghy et al., 2022) and mantle-scale (e.g., Haynie & Jadamec, 2017; Jadamec & Billen, 2010, 2012; Jadamec et al., 2013) geodynamical models of subduction in Alaska and its impact on the overriding continental lithosphere. The crustal seismic velocities and thickness constraints synthesized in this study could also help to better design representative models of upper plate dynamics (Torne et al., 2019) and models of plateau subduction to examine the effects of plateau subduction collision on long-term plate boundary evolution (e.g., Haynie, 2019; Koons et al., 2010; Moresi et al., 2014) and the role of eclogitization of the subducting plateau with depth (Arrial & Billen, 2013).

6.6. CONCLUSIONS

A primary goal of this study was to synthesize the results of existing seismic studies to create tools for studying the upper plate lithosphere in Alaska that could be used by a broad range of researchers. To that end, this study provides:

- maps showing the results of seven studies of crustal thickness based on receiver functions;
- a crustal thickness reference map that synthesizes the three of these crustal thickness models that provided at least semicontinuous sampling and that accounts for complexity due to multiple crustal layers in southern Alaska;
- maps of eight published shear-velocity models for Alaska;
- domain boundaries determined through clustering analysis and their corresponding velocity profiles from the individual shear-velocity models; and
- composite domain boundaries and mean velocity profiles that represent the combination of all shear-velocity models.

Through the clustering analysis, six distinct velocity domains are identified in the crustal depth range (10–50 km) and in the mantle (40–120 km), without considering information on the distribution of terranes and faults. However, the velocity domain boundaries are in many cases close to terrane boundaries and/or major fault systems, indicating feedback between the crust (and even mantle structure) and geologic features at the surface. These correlations include both crust and

mantle domain boundaries that align with the Denali Fault System and the boundary between the Wrangellia composite terrane and interior Alaska, the Kobuk fault and the southern boundary of the Hammond-Coldfoot subterrane in northern Alaska, the southern boundary of the North Slope subterrane in northern Alaska, and the Porcupine Shear Zone in northern Alaska. The Kaltag Fault and the Tintina Fault at least partially align with the crustal and mantle velocity domain boundaries, respectively.

The crust and mantle velocity domains clearly outline three major structural domains within the upper plate of Alaska: the anomalously thick crust associated with the subduction of the Yakutat terrane in the south, the thin lithosphere above a well-defined low-velocity lithosphere over much of interior Alaska, an anomalously thick crust and a transition to thicker lithosphere beneath the Brooks Range, and a thick crust above very thick and high-velocity mantle lithosphere beneath the North Slope subterrane in northernmost Alaska. The western edge of the thick lithosphere beneath the MacKenzie craton in Canada is also detected as a mantle domain boundary.

ACKNOWLEDGMENTS

This chapter grew out of discussions at the UNAVCO Alaska EarthScope and Beyond Virtual Seminar Series in Spring 2021 and the paired EarthScope Alaska and Beyond Virtual Workshop in May 2021, which were supported by the National Science Foundation and the National Aeronautics and Space Administration. The authors thank the conference organizers, Jeffrey Freymueller, Julie Elliot, Sarah Roeske, and Rick Aster, and participants at the meeting for thoughtful discussions. We are also grateful to R. Martin-Short, M. Miller, and A. Li for directly providing their models, to the other authors who made their models available through the IRIS EMC, and to the field teams for deploying and maintaining the seismic networks used to produce the synthesized seismic models. We appreciate the constructive comments from Natalia Ruppert, Xueyang Bao, Carl Tape, and an anonymous reviewer that significantly improved the manuscript. X. Yang thanks Chuanming Liu for providing the script to plot the tectonic terranes in Figures 6.1b and 6.13. This work is supported by the startup funding of Purdue University to X. Yang, NSF CAREER Award NSF-EAR 1945513 to M. Jadamec, NSF EAR-2052558 to S. S. Wei, NSF EAR-2053042 and Woods Hole Oceanographic Institution OBS Instrument Center Postdoctoral Scholarship to M. E. Mann, and NSF EAR-1829401 to K. M. Fischer.

AUTHOR CONTRIBUTIONS

X. Yang contributed to supervision, funding acquisition, data curation, methodology, formal analysis, interpretation, and writing of the original draft. M. Mann and K. Fischer contributed to data curation, methodology, formal analysis, interpretation, and writing of the original draft. M. Jadamec contributed to the contextual outlining and writing of the original draft. S. Wei and A. Schaeffer contributed to methodology. G. Pavlis contributed to formal analysis. All authors contributed to the conceptualization, interpretation, and reviewing and editing of the manuscript.

AVAILABILITY STATEMENT

Seismic network information is available from the IRIS Data Management Center (https://ds.iris.edu/ds/nodes/dmc/) and the International Federation of Digital Seismograph Networks (https://www.fdsn.org). The network codes and digital object identifiers (DOI) are: 5C (DOI: 10.7914/SN/5C_2009), 7C (DOI:10.7914/SN/7C_2015), AK (DOI:10.7914/SN/AK), AT (DOI:10.7914/SN/AT), AV (DOI:10.7914/SN/AV), CN (DOI:10.7914/SN/CN), II (DOI:10.7914/SN/II), IM (no DOI), IU (DOI:10.7914/SN/IU), PP (no DOI), PQ (DOI:10.7914/SN/PQ), TA (DOI:10.7914/SN/TA), US (DOI:10.7914/SN/US), XE (DOI:10.7914/SN/XE_1999), XF (DOI:10.7914/SN/XF_2009), XL (DOI:10.7914/SN/XL_2008), XM (DOI:10.7914/SN/XM_2011), XN (DOI:10.7914/SN/XN_2003), XO (DOI:10.7914/SN/XO_2018), XR (DOI:10.7914/SN/XR_2004), XV (DOI:10.7914/SN/XV_2014), XZ (DOI:10.7914/SN/XZ_2005), YE (DOI:10.7914/SN/YE_2007), YG (DOI:10.7914/SN/YG_2016), YM (DOI:10.7914/SN/YM_2002), YO (DOI:10.7914/SN/YO_2010), YV (DOI:10.7914/SN/YV_2006), Z5 (DOI:10.7914/SN/Z5_2018), ZE (DOI:10.7914/SN/ZE_2015). See Table 6.S1 on the companion website for detailed descriptions and references of the seismic networks. The seismic models are downloaded from IRIS Earth Model Collaboration (https://doi.org/10.17611/DP/EMC.1) or directly provided by the corresponding authors. The clustering analysis of the seismic velocity models is conducted using *SeisGo* (https://doi.org/10.5281/zenodo.5873724). Figures 6.1, 6.2, 6.5, 6.6, 6.11, and 6.13 are created using the Generic Mapping Tools (Wessel et al., 2019). The electronic supplementary file for Figures 6.S1–6.S9 and Table 6.S1, the velocity domain outlines, the key cluster boundaries (cluster lineaments), the average crustal thickness models, and the Python Jupyter notebook to plot the cluster domains are archived on Zenodo and can be downloaded from https://doi.org/10.5281/zenodo.7516572.

REFERENCES

Ai, Y., Zhao, D., Gao, X., & Xu, W. (2005, June). The crust and upper mantle discontinuity structure beneath Alaska inferred from receiver functions. *Physics of the Earth and Planetary Interiors*, *150*, 339–350. doi: 10.1016/J.PEPI.2004.12.002

Allam, A. A., Schulte-Pelkum, V., Ben-Zion, Y., Tape, C., Ruppert, N., & Ross, Z. E. (2017, November). Ten kilometer vertical Moho offset and shallow velocity contrast along the Denali fault zone from double-difference tomography, receiver functions, and fault zone head waves. *Tectonophysics*, *721*, 56–69. doi: 10.1016/J.TECTO.2017.09.003

Anderson, D. L. (1987, May). A seismic equation of state II. Shear properties and thermodynamics of the lower mantle. *Physics of the Earth and Planetary Interiors*, *45*, 307–323. Retrieved from https://linkinghub.elsevier.com/retrieve/pii/0031920187900392 doi: 10.1016/0031-9201(87)90039-2

Arrial, P.-A., & Billen, M. I. (2013). Influence of geometry and eclogitization on oceanic plateau subduction. *Earth and Planetary Science Letters*, *363*, 34–43.

Audet, P., Currie, C. A., Schaeffer, A. J., & Hill, A. M. (2019). Seismic evidence for lithospheric thinning and heat in the northern Canadian Cordillera. *Geophysical Research Letters*, *46* (8), 4249–4257.

Audet, P., Schutt, D. L., Schaeffer, A. J., Estève, C., Aster, R. C., & Cubley, J. F. (2020, November). Moho Variations across the Northern Canadian Cordillera. *Seismological Research Letters*, *91*, 3076–3085. doi: 10.1785/0220200166

Avé Lallemant, H. G., Gottschalk, R. R., Sisson, V. B., & Oldow, J. S. (1998). Structural analysis of the Kobuk fault zone, north-central Alaska. *Special Paper of the Geological Society of America*, *324*, 261–268. doi: 10.1130/0-8137-2324-8.261

Barcheck, G., Abers, G. A., Adams, A. N., Bécel, A., Collins, J., Gaherty, J. B., et al. (2020, November). The Alaska Amphibious Community Seismic Experiment. *Seismological Research Letters*, *91*, 3054–3063. doi: 10.1785/0220200189

Batir, J. F., Blackwell, D. D., & Richards, M. C. (2016). Heat flow and temperature-depth curves throughout Alaska: Finding regions for future geothermal exploration. *Journal of Geophysics and Engineering*, *13*, 366–377. doi: 10.1088/1742-2132/13/3/366

Bauer, M. A., Pavlis, G. L., & Landes, M. (2014). Subduction geometry of the Yakutat terrane, southeastern Alaska. *Geosphere*, *10*, 1161–1176. doi: 10.1130/GES00852.1

Benowitz, J. A., Roeske, S. M., Regan, S. P., Waldien, T. S., Elliott, J. L., & O'Sullivan, P. B. (2022, June). Large-scale, crustal-block vertical extrusion between the Hines Creek and Denali faults coeval with slip localization on the Denali fault since ca. 45 Ma, Hayes Range, Alaska, USA. *Geosphere*, *18*, 1030–1054. Retrieved from https://doi.org/10.1130/GES02466.1. doi: 10.1130/GES02466.1

Berg, E. M., Lin, F. C., Allam, A., Schulte-Pelkum, V., Ward, K. M., & Shen, W. (2020, February). Shear velocity model of Alaska via joint inversion of rayleigh wave ellipticity, phase velocities, and receiver functions across the Alaska transportable array. *Journal of Geophysical Research: Solid Earth*, *125*, e2019JB018582. Retrieved from https://onlinelibrary.wiley.com/doi/full/10.1029/2019JB018582 doi: 10.1029/2019JB018582

Bird, P. (1996). Computer simulations of Alaskan tectonics. *Tectonics*, *15*(2), 225–236.

Bird, P. (2003). An updated digital model of plate boundaries. *Geochemistry Geophysics Geosystems*, *4*(3), 1027. doi: 10.1029/2001GC000252

Bostock, M. G. (2013, December). The Moho in subduction zones. *Tectonophysics*, *609*, 547–557. doi: 10.1016/J.TECTO.2012.07.007

Brennan, P. R. K., Gilbert, H., Ridgway, K. D., Brennan, P. R. K., Gilbert, H., Ridgway, K. D. (2011, April). Crustal structure across the central Alaska range: Anatomy of a mesozoic collisional zone. *Geochemistry, Geophysics, Geosystems*, *12*, 4010. Retrieved from https://onlinelibrary.wiley.com/doi/full/10.1029/2011GC003519 doi: 10.1029/2011GC003519

Chuang, L., Bostock, M., Wech, A., & Plourde, A. (2017, July). Plateau subduction, intraslab seismicity, and the Denali (Alaska) volcanic gap. *Geology*, *45*, 647–650. Retrieved from https://pubs.geoscienceworld.org/geology/article/45/7/647-650/207873 doi: 10.1130/G38867.1

Clarke, T. J., & Silver, P. G. (1991, January). A procedure for the systematic interpretation of body wave seismograms—I. Application to Moho depth and crustal properties. *Geophysical Journal International*, *104*, 41–72. Retrieved from https://academic.oup.com/gji/article/104/1/41/569865 doi: 10.1111/J.1365-246X.1991.TB02493.X

Colpron, M., Nelson, J. L., & Murphy, D. C. (2007, April). Northern Cordilleran terranes and their interactions through time. *GSA Today*, *17*, 4. Retrieved from http://www.geosociety.org/gsatoday/archive/17/4/pdf/i1052-5173-17-4-4.pdf doi: 10.1130/GSAT01704-5A.1

Coney, P. J., Jones, D. L., & Monger, J. W. (1980). Cordilleran suspect terranes. *Nature*, *288*(5789), 329–333. Retrieved from http://www.nature.com/articles/288329a0 doi: 10.1038/288329a0.

Daly, K. A., Abers, G. A., Mann, M. E., Roecker, S., & Christensen, D. H. (2021, November). Subduction of an oceanic plateau across southcentral Alaska: High-resolution seismicity. *Journal of Geophysical Research: Solid Earth*, *126*. Retrieved from https://onlinelibrary.wiley.com/doi/10.1029/2021JB022809 doi: 10.1029/2021JB022809

Dayem, K. E., Houseman, G. A., & Molnar, P. (2009, June). Localization of shear along a lithospheric strength discontinuity: Application of a continuous deformation model to the boundary between Tibet and the Tarim Basin. *Tectonics*, *28*. Retrieved from https://onlinelibrary.wiley.com/doi/full/10.1029/2008TC002264 doi: 10.1029/2008TC002264

Delph, J. R., Shimizu, K., & Ratschbacher, B. C. (2021, July). The architecture of the southern Puna Magmatic System: Integrating seismic and petrologic observations with geochemical modeling. *Journal of Geophysical Research: Solid Earth*, *126*, e2020JB021550. Retrieved from https://onlinelibrary.wiley.com/doi/full/10.1029/2020JB021550 doi: 10.1029/2020JB021550

DeMets, C., Gordon, R. G., Argus, D. F., & Stein, S. (1994). Effect of recent revisions to the geomagnetic reversal time scale on estimates of current plate motions. *Geophysical Research Letters*, *218*(207–237), 2191–2194.

Eberhart-Phillips, D., Christensen, D. H., Brocher, T. M., Dutta, U., Hansen, R. J., & Ratchkovski, N. A. (2004).

Imaging the transition from Aleutian subduction to Yakutat collision in central Alaska, with local earthquakes and active source data. *Geological Society of New Zealand Miscellaneous Publication*, *117A*, 27.

Eberhart-Phillips, D., Christensen, D. H., Brocher, T. M., Hansen, R., Ruppert, N. A., Haeussler, P. J., & Abers, G. A. (2006). Imaging the transition from Aleutian subduction to Yakutat collision in central Alaska, with local earthquakes and active source data. *Journal of Geophysical Research: Solid Earth*, *111*, 1–31. doi: 10.1029/2005JB004240

Elliott, J., & Freymueller, J. T. (2020). A block model of present-day kinematics of Alaska and western Canada. *Journal of Geophysical Research: Solid Earth*, *125*, 1–30. doi: 10.1029/2019JB018378

Enkelmann, E., Zeitler, P., Garver, J., Pavlis, T., & Hooks, B. (2010). The thermochronological record of tectonic and surface process interaction at the Yakutat–North American collision zone in southeast Alaska. *American Journal of Science*, *310*(4), 231–260.

Esteve, C., Audet, P., Schaeffer, A. J., Schutt, D., Aster, R. C., & Cubley, J. (2020). The upper mantle structure of northwestern Canada from teleseismic body wave tomography. *Journal of Geophysical Research: Solid Earth*, *125*(2).

Esteve, C., Gosselin, J., Audet, P., Schaeffer, A. J., Schutt, D., & Aster, R. C. (2021). Surface-wave tomography of the Northern Canadian Cordillera using earthquake Rayleigh wave group velocities. *Journal of Geophysical Research: Solid Earth*, *126*, e2021JB021960. Retrieved from https://doi.org/10.1029/2021JB021960

Eymold, W. K., & Jordan, T. H. (2019, November). Tectonic regionalization of the southern California crust from tomographic cluster analysis. *Journal of Geophysical Research: Solid Earth*, *124*, 11840–11865. Retrieved from https://agupubs.onlinelibrary.wiley.com/doi/10.1029/2019JB018423 doi: 10.1029/2019JB018423

Falkowski, S., & Enkelmann, E. (2016, August). Upper-crustal cooling of the Wrangellia composite terrane in the northern St. Elias Mountains, western Canada. *Lithosphere*, *8*, 359–378. Retrieved from http://pubs.geoscienceworld.org/gsa/lithosphere/article-pdf/8/4/359/3040051/359.pdf doi: 10.1130/L508.1

Feng, L., & Ritzwoller, M. H. (2019). A 3-D shear velocity model of the crust and uppermost mantle beneath Alaska including apparent radial anisotropy. *Journal of Geophysical Research: Solid Earth*, *124*, 10468–10497. doi: 10.1029/2019JB018122

Finzel, E. S., Flesch, L. M., Ridgway, K. D., Holt, W. E., & Ghosh, A. (2015). Surface motions and intraplate continental deformation in Alaska driven by mantle flow. *Geophysical Research Letters*, *42*(11), 4350–4358.

Fuis, G. S., Levander, A. R., Lutter, W. J., Wissinger, E. S., Moore, T. E., & Christensen, N. I. (1995). Seismic images of the Brooks Range, Arctic Alaska, reveal crustal-scale duplexing. *Geology*, *23*, 65–68. Retrieved from http://pubs.geoscienceworld.org/gsa/geology/article-pdf/23/1/65/4665573/i0091-7613-23-1-65.pdf

Fuis, G. S., Moore, T. E., Plafker, G., Brocher, T. M., Fisher, M. A., Mooney, W. D. et al. (2008). Trans-Alaska Crustal Transect and continental evolution involving subduction underplating and synchronous foreland thrusting. *Geology*, *36*, 267–270. doi: 10.1130/G24257A.1

Fuis, G. S., Murphy, J. M., Lutter, W. J., Moore, T. E., Bird, K. J., & Christensen, N. I. (1997, September). Deep seismic structure and tectonics of northern Alaska: Crustal-scale duplexing with deformation extending into the upper mantle. *Journal of Geophysical Research: Solid Earth*, *102*, 20873–20896. Retrieved from https://onlinelibrary.wiley.com/doi/full/10.1029/96JB03959 doi: 10.1029/96JB03959

Fuis, G. S., & Plafker, G. (1991, March). Evolution of deep structure along the Trans-Alaska Crustal Transect, Chugach Mountains and Copper River Basin, southern Alaska. *Journal of Geophysical Research: Solid Earth*, *96*, 4229–4253. Retrieved from https://onlinelibrary.wiley.com/doi/full/10.1029/90JB02276 doi: 10.1029/90JB02276

Gabrielse, H., Murphy, D. C., & Mortensen, J. K. (2006). Cretaceous and Cenozoic dextral orogen-parallel displacements, magmatism, and paleogeography, north-central Canadian Cordillera. In J. Haggart & J. E. R.J. Monger (Eds.), *Paleogeography of the north American cordillera: Evidence for and against large-scale displacements: Geological association of Canada special paper* (Vol. *46*, pp. 255–276). Retrieved from https://www.researchgate.net/publication/285873017

Gama, I., Fischer, K. M., Dalton, C. A., & Eilon, Z. (2022, December). Variations in Lithospheric Thickness across the Denali Fault and in Northern Alaska. *Geophysical Research Letters*, e2022GL101256. Retrieved from https://onlinelibrary.wiley.com/doi/full/10.1029/2022GL101256 doi: 10.1029/2022GL101256

Gama, I., Fischer, K. M., Eilon, Z., Krueger, H. E., Dalton, C. A., & Flesch, L. M. (2021, April). Shear-wave velocity structure beneath Alaska from a Bayesian joint inversion of Sp receiver functions and Rayleigh wave phase velocities. *Earth and Planetary Science Letters*, *560*, 116785. doi: 10.1016/J.EPSL.2021.116785

Gama, I., Fischer, K. M., & Hua, J. (2022, October). Mapping the lithosphere and asthenosphere beneath Alaska with Sp converted waves. *Geochemistry, Geophysics, Geosystems*, *23*, e2022GC010517. Retrieved from https://onlinelibrary.wiley.com/doi/10.1029/2022GC010517 doi: 10.1029/2022GC010517

Gou, T., Zhao, D., Huang, Z., & Wang, L. (2019). Aseismic deep slab and mantle flow beneath Alaska: Insight from anisotropic tomography. *Journal of Geophysical Research: Solid Earth*, *124*, 1700–1724. doi: 10.1029/2018JB016639

Grantz, A., May, S. D., & Hart, P. E. (1994). Geology of the Arctic continental margin of Alaska. In *The Geology of Alaska* (Vols. DNAG, Geology of North America). Geological Society of America. doi: 10.1130/DNAG-GNA-G1.17

Haney, M. M., Ward, K. M., Tsai, V. C., & Schmandt, B. (2020, November). Bulk structure of the crust and upper mantle beneath Alaska from an approximate Rayleigh-wave dispersion formula. *Seismological Research Letters*, *91*, 3064–3075. Retrieved from https://pubs.geoscienceworld.org/ssa/srl/article/91/6/3064/589671/Bulk-Structure-of-the-Crust-and-Upper-Mantle doi: 10.1785/0220200162

Hayes, G. P., Moore, G. L., Portner, D. E., Hearne, M., Flamme, H., Furtney, M., & Smoczyk, G. M. (2018). Slab2,

a comprehensive subduction zone geometry model. *Science*, *362*, 58–61. doi: 10.1126/science.aat4723

Haynie, K. L. (2019). *Controls of flat slab versus oceanic plateau subduction on overriding plate deformation in south-central Alaska* (Unpublished doctoral dissertation). State University of New York at Buffalo.

Haynie, K. L., & Jadamec, M. A. (2017, July). Tectonic drivers of the Wrangell block: Insights on fore-arc sliver processes from 3-D geodynamic models of Alaska. *Tectonics*, *36*, 1180–1206. Retrieved from https://onlinelibrary.wiley.com/doi/10.1002/2016TC004410 doi: 10.1002/2016TC004410

Hubbard, R. J., Edrich, S. P., & Rattey, R. P. (1987, February). Geologic evolution and hydrocarbon habitat of the "Arctic Alaska Microplate". *Marine and Petroleum Geology*, *4*, 2–34. doi: 10.1016/0264-8172(87)90019-5

Hyndman, R. D., Currie, C. A., & Mazzotti, S. P. (2005). Subduction zone backarcs, mobile belts, and orogenic heat. *Geological Society of America Today*, *15*(23). doi: 10:1130/1052-5173

Jadamec, M. A., & Billen, M. I. (2010). Reconciling surface plate motions and rapid three-dimensional flow around a slab edge. *Nature*, *465*, 338–342.

Jadamec, M. A., & Billen, M. I. (2012). The role of rheology and slab shape on rapid mantle flow: Three-dimensional numerical models of the Alaska slab edge. *Journal of Geophysical Research: Solid Earth*, *117*, 1–20. doi: 10.1029/2011JB008563

Jadamec, M. A., Billen, M. I., & Roeske, S. M. (2013). Three-dimensional numerical models of flat slab subduction and the Denali fault driving deformation in south-central Alaska. *Earth and Planetary Science Letters*, *376*, 29–42. Retrieved from http://dx.doi.org/10.1016/j.epsl.2013.06.009 doi: 10.1016/j.epsl.2013.06.009

Jiang, C., Schmandt, B., Ward, K. M., Lin, F., & Worthington, L. L. (2018, October). Upper mantle seismic structure of Alaska from Rayleigh and S wave tomography. *Geophysical Research Letters*, *45*, 10,350–10,359. Retrieved from https://onlinelibrary.wiley.com/doi/10.1029/2018GL079406 doi: 10.1029/2018GL079406

Jones, P. B. (1980). Evidence from Canada and Alaska on plate tectonic evolution of the Arctic Ocean Basin. *Nature*, *285*, 215–217. Retrieved from https://www.nature.com/articles/285215a0 doi: 10.1038/285215a0

Kalbas, J. L., Freed, A. M., & Ridgway, K. D. (2008). Contemporary fault mechanics in southern Alaska. *Geophysical Monograph Series*, *179*, 321–336.

Kim, Y., Abers, G. A., Li, J., Christensen, D., Calkins, J., & Rondenay, S. (2014, March). Alaska Megathrust 2: Imaging the megathrust zone and Yakutat/Pacific plate interface in the Alaska subduction zone. *Journal of Geophysical Research: Solid Earth*, *119*, 1924–1941. Retrieved from https://onlinelibrary.wiley.com/doi/full/10.1002/2013JB010581 doi: 10.1002/2013JB010581

Koehler, R., & Carver, G. (2018, May). Active faults and seismic hazards in Alaska. In *Alaska Division of Geological and Geophysical Surveys Miscellaneous Publication* (Vol. *160*, 59p). doi: 10.14509/29705

Koons, P. O., Hooks, B. P., Pavlis, T., Upton, P., & Barker, A. D. (2010, August). Three-dimensional mechanics of Yakutat convergence in the southern Alaskan plate corner. *Tectonics*, *29*. Retrieved from https://agupubs.onlinelibrary.wiley.com/doi/10.1029/2009TC002463 doi: 10.1029/2009TC002463

Lahr, J. C., & Plafker, G. (1980). Holocene Pacific-North American plate interaction in southern Alaska: implications for the Yakataga seismic gap. *Geology*, *8*, 483–486.

Langston, C. A. (1977, June). Corvallis, oregon, crustal and upper mantle receiver structure from teleseismic p and s waves. *Bulletin of the Seismological Society of America*, *67*, 713–724. doi: 10.1785/BSSA0670030713

Lekic, V., & Romanowicz, B. (2011, August). Tectonic regionalization without a priori information: A cluster analysis of upper mantle tomography. *Earth and Planetary Science Letters*, *308*, 151–160. doi: 10.1016/J.EPSL.2011.05.050

Liu, C., Zhang, S., Sheehan, A. F., & Ritzwoller, M. H. (2022, November). Surface wave isotropic and azimuthally anisotropic dispersion across Alaska and the Alaska-Aleutian subduction zone. *Journal of Geophysical Research: Solid Earth*, *127*, e2022JB024885. Retrieved from https://onlinelibrary.wiley.com/doi/10.1029/2022JB024885 doi: 10.1029/2022JB024885

Mann, M. E., Abers, G. A., Daly, K. A., & Christensen, D. H. (2022, January). Subduction of an oceanic plateau across southcentral Alaska: Scattered-wave imaging. *Journal of Geophysical Research: Solid Earth*, *127*. doi: 10.1029/2021JB022697

Martin-Short, R., Allen, R., Bastow, I. D., Porritt, R. W., & Miller, M. S. (2018, November). Seismic imaging of the Alaska subduction zone: Implications for slab geometry and volcanism. *Geochemistry, Geophysics, Geosystems*, *19*, 4541–4560. Retrieved from https://onlinelibrary.wiley.com/doi/10.1029/2018GC007962 doi: 10.1029/2018GC007962

McConeghy, J., Flesch, L., & Elliott, J. (2022, October). Investigating the effect of mantle flow and viscosity structure on surface velocities in Alaska using 3-D geodynamic models. *Journal of Geophysical Research: Solid Earth*, *127*. Retrieved from https://onlinelibrary.wiley.com/doi/10.1029/2022JB024704 doi: 10.1029/2022JB024704

Miller, M. S., & Moresi, L. (2018, November). Mapping the Alaskan moho. *Seismological Research Letters*, *89*, 2430–2436. doi: 10.1785/0220180222

Miller, M. S., O'Driscoll, L. J., Porritt, R. W., & Roeske, S. M. (2018). Multiscale crustal architecture of Alaska inferred from p receiver functions. *Lithosphere*, *10*, 267–278. doi: 10.1130/L701.1

Molnar, P., & Dayem, K. E. (2010, August). Major intracontinental strike-slip faults and contrasts in lithospheric strength. *Geosphere*, *6*, 444–467. Retrieved from http://pubs.geoscienceworld.org/gsa/geosphere/article-pdf/6/4/444/3338959/444.pdf doi: 10.1130/GES00519.1

Moore, T. E., & Box, S. E. (2016). Age, distribution and style of deformation in Alaska north of 60 n: Implications for assembly of Alaska. *Tectonophysics*, *691*, 133–170.

Moresi, L., Betts, P., Miller, M., & Cayley, R. (2014). Dynamics of continental accretion. *Nature*, *508*(7495), 245–248.

Mukasa, S. B., Andronikov, A. V., & Hall, C. M. (2007). The 40Ar/39Ar chronology and eruption rates of Cenozoic volcanism in the eastern Bering Sea Volcanic Province, Alaska. *Journal of Geophysical Research: Solid Earth*, *112*(B6). Retrieved from https://agupubs.onlinelibrary.wiley.com/

doi/abs/10.1029/2006JB004452 doi: https://doi.org/10.1029/2006JB004452

Müller, R. D., Zahirovic, S., Williams, S. E., Cannon, J., Seton, M., Bower, D. J., et al. (2019). A global plate model including lithospheric deformation along major rifts and orogens since the Triassic. *Tectonics*, *38*(6), 1884–1907.

Nayak, A., Eberhart-Phillips, D., Ruppert, N. A., Fang, H., Moore, M. M., Tape, C., et al. (2020, November). 3D seismic velocity models for Alaska from joint tomographic inversion of body-wave and surface-wave data. *Seismological Research Letters*, *91*, 3106–3119. Retrieved from http://pubs.geoscienceworld.org/ssa/srl/article-pdf/91/6/3106/5176960/srl-2020214.1.pdf doi: 10.1785/0220200214

Nokleberg, W., Aleinikoff, J., Bundtzen, T., & Hanshaw, M. (2013). *Geologic strip map along the Hines Creek Fault showing evidence for Cenozoic displacement in the western Mount Hayes and northeastern Healy quadrangles, eastern Alaska Range, Alaska* (Tech. Rep.). Retrieved from https://pubs.usgs.gov/sim/3238/

Nokleberg, W. J., MollStalcup, E., Miller, T., Brew, D., Grantz, A., Reed, J., Jr., et al. (1994). *Tectonostratigraphic terrane and overlap assemblage map of Alaska*. US Geological Survey, Open-File Report 94-194.

O'Driscoll, L. J., & Miller, M. S. (2015, April). Lithospheric discontinuity structure in Alaska, thickness variations determined by sp receiver functions. *Tectonics*, *34*, 694–714. doi: 10.1002/2014TC003669

Pavlis, G. L., Bauer, M. A., Elliott, J. L., Koons, P., Pavlis, T. L., Ruppert, N., et al. (2019). A unified three-dimensional model of the lithospheric structure at the subduction corner in southeast Alaska: Summary results from steep. *Geosphere*, *15*, 382–406. doi: 10.1130/GES01488.1

Pavlis, T. L., Amato, J. M., Trop, J. M., Ridgway, K. D., Roeske, S. M., & Gehrels, G. E. (2019). Subduction polarity in ancient arcs; a call to integrate geology and geophysics to decipher the Mesozoic tectonic history of the Northern Cordillera of North America. *GSA Today*, *29*(11), 4–10.

Plafker, G., & Berg, H. C. (1994, April). Overview of the geology and tectonic evolution of Alaska. In (pp. 989–1021). Geological Society of America. Retrieved from https://pubs.geoscienceworld.org/books/book/875/chapter/4867358/ doi: 10.1130/DNAG-GNA-G1.989

Plafker, G., Gilpin, L. M., & Lahr, J. C. (1994). Plate 12: Neotectonic Map of Alaska. In G. Plafker & H. Berg (Eds.), *The Geology of North America* (Vols. G1, The Geology of Alaska). Boulder, CO: Geological Society of America.

Plafker, G., Hudson, T., Bruns, T., & Rubin, M. (1978). Late Quaternary offsets along the Fairweather fault and crustal plate interactions in southern Alaska. *Canadian Journal of Earth Sciences*, *15*(5), 805–816. Retrieved from https://doi.org/10.1139/e78-085 doi: 10.1139/e78-085

Plafker, G., Moore, J. C., & Winkler, G. R. (1994). Geology of the southern Alaska margin. In G. Plafker & H. Berg (Eds.), *The Geology of North America* (Vols. G1, The Geology of Alaska, pp. 389–449). Boulder, CO.: Geological Society of America.

Rondenay, S., Abers, G. A., & van Keken, P. E. (2008, April). Seismic imaging of subduction zone metamorphism. *Geology*, *36*, 275–278. doi: 10.1130/G24112A.1

Rondenay, S., Montési, L. G., & Abers, G. A. (2010, August). New geophysical insight into the origin of the Denali volcanic gap. *Geophysical Journal International*, *182*, 613–630. Retrieved from https://academic.oup.com/gji/article/182/2/613/568363 doi: 10.1111/J.1365-246X.2010.04659.X

Rossi, G., Abers, G. A., Rondenay, S., & Christensen, D. H. (2006, September). Unusual mantle poisson's ratio, subduction, and crustal structure in central Alaska. *Journal of Geophysical Research: Solid Earth*, *111*, 9311. Retrieved from https://onlinelibrary.wiley.com/doi/full/10.1029/2005JB003956 doi: 10.1029/2005JB003956

Ruppert, N. A., & West, M. E. (2020, March). The impact of USArray on earthquake monitoring in Alaska. *Seismological Research Letters*, *91*, 601–610. doi: 10.1785/0220190227

Schaeffer, A. J., & Lebedev, S. (2015, January). Global heterogeneity of the lithosphere and underlying mantle: A seismological appraisal based on multimode surface-wave dispersion analysis, shear-velocity tomography, and tectonic regionalization. *The Earth's heterogeneous mantle: A geophysical, geodynamical, and geochemical perspective* (pp. 3–46). Retrieved from https://link.springer.com/chapter/10.1007/978-3-319-15627-9 1 doi: 10.1007/978-3-319-15627-9 1/FIGURES/19

Schulte-Pelkum, V., Caine, J. S., Jones, J. V., & Becker, T. W. (2020, November). Imaging the tectonic grain of the Northern Cordillera Orogen using Transportable Array receiver functions. *Seismological Research Letters*, *91*, 3086–3105. doi: 10.1785/0220200182

Searcy, C. K., Christensen, D. H., & Zandt, G. (1996, February). Velocity structure beneath college station Alaska from receiver functions. *Bulletin of the Seismological Society of America*, *86*, 232–241. doi: 10.1785/BSSA08601A0232

Seton, M., Müller, R. D., Zahirovic, S., Williams, S., Wright, N. M., Cannon, J., et al. (2020). A global data set of present-day oceanic crustal age and seafloor spreading parameters. *Geochemistry, Geophysics, Geosystems*, *21*(10), e2020GC009214.

Sharples, W., Jadamec, M. A., Moresi, L. N., & Capitanio, F. (2014). Overriding plate controls on subduction evolution. *Journal of Geophysical Research*, *119*, 6684–6704. doi: 10.1002/2014JB011163

Silberling, N. J., Jones, D. L., Monger, J. W. H., Coney, P. J., Berg, H. C., & Plafker, G. (1994). Plate 3: Lithotectonic terrane map of Alaska and adjacent parts of Canada. In G. Plafker & H. Berg (Eds.), *The Geology of North America* (Vols. G1, The Geology of Alaska). Boulder, CO.: Geological Society of America.

Strauss, J. V., Macdonald, F. A., Taylor, J. F., Repetski, J. E., & McClelland, W. C. (2013). Laurentian origin for the North Slope of Alaska: Implications for the tectonic evolution of the arctic. *Lithosphere*, *5*, 477–482. doi: 10.1130/L284.1

Tavenard, R., Faouzi, J., Vandewiele, G., Divo, F., Androz, G., Holtz, C., et al. (2020). Tslearn, A Machine Learning Toolkit for Time Series Data. *Journal of Machine Learning Research*, *21*(118), 1–6. Retrieved from http://jmlr.org/papers/v21/20-091.html

Torne, M., Jimenez-Munt, I., Verges, J., Fernandez, M., Carballo, A., & Jadamec, M. A. (2019). Regional crustal and lithospheric thickness model for Alaska, the Chukchi Shelf,

and the inner and outer Bering Shelves. *Geophysical Journal International*, *ggz424*. doi: https://doi.org/10.1093/gji/ggz424

Tozer, B., Sandwell, D. T., Smith, W. H., Olson, C., Beale, J., & Wessel, P. (2019). Global bathymetry and topography at 15 arc sec: Srtm15+. *Earth and Space Science*, *6*(10), 1847–1864.

Veenstra, E., Christensen, D. H., Abers, G. A., & Ferris, A. (2006, November). Crustal thickness variation in south-central Alaska. *Geology*, *34*, 781–784. doi: 10.1130/G22615.1

von Gosen, W., Piepjohn, K., McClelland, W., & Colpron, M. (2019, June). Evidence for the sinistral Porcupine shear zone in North Yukon (Canadian Arctic) and geotectonic implications. In Circum-Arctic Structural Events: Tectonic Evolution of the Arctic Margins and Trans-Arctic Links with Adjacent Orogens (pp. 473–491). Geological Society of America. doi: 10.1130/2019.2541(21)

Ward, K. M., & Lin, F. C. (2018). Lithospheric structure across the Alaskan cordillera from the joint inversion of surface waves and receiver functions. *Journal of Geophysical Research: Solid Earth*, *123*, 8780–8797. doi: 10.1029/2018JB015967

Wessel, P., Luis, J. F., Uieda, L., Scharroo, R., Wobbe, F., Smith, W. H. F., & Tian, D. (2019, November). The Generic Mapping Tools Version 6. *Geochemistry, Geophysics, Geosystems*, *20*, 5556–5564. doi: 10.1029/2019GC008515

Woollard, G. P., Ostenso, N. A., Thiel, E., & Bonini, W. E. (1960, March). Gravity anomalies, crustal structure, and geology in Alaska. *Journal of Geophysical Research*, *65*, 1021–1037. Retrieved from http://doi.wiley.com/10.1029/JZ065i003p01021 doi: 10.1029/JZ065i003p01021

Yang, X., Bryan, J., Okubo, K., Jiang, C., Clements, T., & Denolle, M. A. (2022, November). Optimal stacking of noise cross-correlation functions. *Geophysical Journal International*, *232*, 1600–1618. Retrieved from https://academic.oup.com/gji/article/232/3/1600/6762921 doi: 10.1093/gji/ggac410

Yang, X., & Gao, H. (2020, November). Segmentation of the Aleutian-Alaska subduction zone revealed by full-wave ambient noise tomography: Implications for the along-strike variation of volcanism. *Journal of Geophysical Research: Solid Earth*, *125*, 1–20. Retrieved from https://onlinelibrary.wiley.com/doi/10.1029/2020JB019677 doi: 10.1029/2020JB019677

Yang, X., Zuffoletti, I. D., D'Souza, N. J., & Denolle, M. A. (2022, January). *SeisGo: A ready-to-go Python toolbox for seismic data analysis* [Computer Software]. Zenodo. Retrieved from https://doi.org/10.5281/zenodo.5873724 doi: 10.5281/zenodo.5873724

Zhang, Y., Li, A., & Hu, H. (2019). Crustal structure in Alaska from receiver function analysis. *Geophysical Research Letters*, *46*, 1284–1292. doi: 10.1029/2018GL081011